

Circular Polarization of Simulated Images of Black Holes

Abhishek V. Joshi^{1,2} , Ben S. Prather^{3,4} , Chi-kwan Chan^{5,6,7} , Maciek Wielgus⁸ , and Charles F. Gammie^{1,2,9,10} 

¹ Department of Physics, University of Illinois, 1110 West Green Street, Urbana, IL 61801, USA

² Illinois Center for Advanced Study of the Universe, 1110 West Green Street, Urbana, IL 61801, USA

³ Department of Physics, University of Illinois at Urbana-Champaign, 1110 West Green Street, Urbana, IL 61801, USA

⁴ Los Alamos National Lab, Los Alamos, NM 87545, USA

⁵ Steward Observatory and Department of Astronomy, University of Arizona, 933 N. Cherry Avenue, Tucson, AZ 85721, USA

⁶ Data Science Institute, University of Arizona, 1230 N. Cherry Avenue, Tucson, AZ 85721, USA

⁷ Program in Applied Mathematics, University of Arizona, 617 N. Santa Rita, Tucson, AZ 85721, USA

⁸ Max-Planck-Institut für Radioastronomie, Auf dem Hügel 69, D-53121 Bonn, Germany

⁹ Department of Astronomy, University of Illinois, 1002 West Green Street, Urbana, IL 61801, USA

¹⁰ National Center for Supercomputing Applications, 605 East Springfield Avenue, Champaign, IL 61820, USA

Received 2024 May 13; revised 2024 June 18; accepted 2024 June 20; published 2024 September 2

Abstract

Models of the resolved Event Horizon Telescope (EHT) sources Sgr A* and M87* are constrained by observations at multiple wavelengths, resolutions, polarizations, and time cadences. In this paper, we compare unresolved circular polarization (CP) measurements to a library of models, where each model is characterized by a distribution of CP over time. In the library, we vary the spin of the black hole, the magnetic field strength at the horizon (i.e., both SANE and magnetically arrested disk or MAD models), the observer inclination, a parameter for the maximum ion-electron temperature ratio assuming a thermal plasma, and the direction of the magnetic field dipole moment. We find that Atacama Large Millimeter/submillimeter Array (ALMA) observations of Sgr A* are inconsistent with all edge-on ($i = 90^\circ$) models. Restricting attention to the MAD models favored by earlier EHT studies of Sgr A*, we find that only models with magnetic dipole moment pointing away from the observer are consistent with ALMA data. We also note that in 26 of the 27 passing MAD models, the accretion flow rotates clockwise on the sky. We provide a table of the means and standard deviations of the CP distributions for all model parameters, along with their trends.

Unified Astronomy Thesaurus concepts: Supermassive black holes (1663); Accretion (14); Low-luminosity active galactic nuclei (2033); Magnetohydrodynamics (1964); Radiative transfer (1335); Polarimetry (1278)

Materials only available in the *online version of record*: machine-readable table

1. Introduction

We investigate the origin of circular polarization (CP) using first-principles models of synchrotron-emitting systems, and study the distribution of the expected CP across a set of models at varying spin, magnetization, and electron distribution functions (eDFs).

The 2017 Event Horizon Telescope (EHT) campaign produced total intensity images of the supermassive black hole at the center of M87 (hereafter, M87*) and the Milky Way (hereafter, Sgr A*) at a resolution of $\sim 25 \mu\text{as}$ (Event Horizon Telescope Collaboration et al. 2019a, 2019b, 2019c, 2019d, 2019e, 2019f—hereafter, EHTC M87 I–VI; and Event Horizon Telescope Collaboration et al. 2022a, 2022b, 2022c, 2022d, 2022e, 2022f—hereafter, EHTC SgrA I–VI). Both reconstructed images show a ring surrounding a central flux depression. The ring is produced by synchrotron emission from hot gas surrounding the black hole, and the central depression corresponds to lines of sight that cross the event horizon (the black hole “shadow”).

EHT images have been interpreted by comparison to a library of numerical models (EHTC M87 V; EHTC SgrA V), in which the spin, flow magnetization, source inclination, and eDF are varied, but the time-averaged 1.3 mm flux density is held fixed and consistent with the 2017 April observations

(EHTC M87 IV; Wielgus et al. 2022a). In particular, plasma flow models were generated using general relativistic magnetohydrodynamics (GRMHD) simulations and then ray-traced using a general relativistic radiative transfer (GRRT) scheme; the modeling procedure is described in detail in Wong et al. (2022). The models predict time-dependent image structure in all four Stokes parameters at frequencies where scattering is unimportant, time-dependent unpolarized flux density across the electromagnetic spectrum, and jet power.

For M87*, the model comparison exercise found a subset of library models that satisfied all available observational constraints. The most discriminating observational constraint was a lower limit on a jet power of $10^{42} \text{ erg s}^{-1}$. The favored models were highly magnetized—so-called magnetically arrested disk (MAD) models (Igumenshchev et al. 2003; Narayan et al. 2003), in which the magnetic flux through the horizon is large enough to episodically push aside the accreting plasma—and contained a population of relatively cool electrons (EHTC M87 V).

For Sgr A*, 11 observational constraints were used in the model comparison exercise. No models satisfied all constraints (EHTC SgrA V). The most discriminating observational constraint was a measure of fractional variability in the 1.3 mm Atacama Large Millimeter/submillimeter Array (ALMA) light curve; almost all models that failed this test were found to be too variable—most models failed with $p < 0.01$ for two-sample Kolmogorov-Smirnov (K-S) tests comparing distributions of the ratio of the standard deviation to mean flux averaged over 3 hr timescales. An incomplete list of possible explanations for this



Original content from this work may be used under the terms of the [Creative Commons Attribution 4.0 licence](#). Any further distribution of this work must maintain attribution to the author(s) and the title of the work, journal citation and DOI.

variability “crisis” is provided in EHTC SgrA **V**, including the possible presence of slowly varying, resolved-out features that would make the fractional variability in the ALMA light curve a lower limit on the variability of the compact source. Setting aside the variability constraint, the Sgr A* model comparison identified a set of models that passed all remaining constraints. The favored models were MAD models that contain a population of relatively cool electrons.

EHT also recorded linear polarization (LP) and CP data in the 2017 campaign. LP and CP model comparison studies of M87* (Event Horizon Telescope Collaboration et al. 2021a, 2021b; hereafter, EHTC M87 VII–VIII) included constraints applied to the models based on LP maps and limits to the total CP fraction. Model LP maps are sensitive to the magnetic field configuration of M87* and are highly constraining. Unresolved CP measurements, by contrast, exclude only a few models.

Event Horizon Telescope Collaboration et al. (2023; hereafter, EHTC M87 IX) analyzed CP in the 2017 EHT campaign data and found evidence for nonzero CP. The Stokes *V* resolved structure could not be constrained, however, in contrast to image reconstructions in Stokes *I*, *Q*, and *U*. EHTC M87 **IX** placed an upper limit on the magnitude of the resolved CP fraction of 3.7%. Consistent with the results from LP model comparisons (EHTC M87 **VIII**), the CP constraints favor highly magnetized simulations with relatively cooler electrons in the disk and jet.

ALMA has recorded polarization data in the 1mm and 3mm bands for Sgr A*, M87*, and other active galactic nuclei (AGNs: low-luminosity AGNs, radio-loud AGNs, and blazars for which horizon-scale images are not possible with the current EHT resolution). Bower et al. (2018; 2016 observations), Goddi et al. (2021), and Wielgus et al. (2022b, 2024; 2017 observations) present this ALMA data with detections or limits on the unresolved LP and CP of Sgr A*. Other unresolved CP observations of Sgr A* from the Submillimeter Array at 3 mm and other wavelengths are given in Muñoz et al. (2012) and references therein.

It is expected that at the observing wavelength of 1.3 mm, emission will be produced by the synchrotron process, which is expected to be strongly linearly polarized. The polarization state is modified, however, by propagation through a warm, magnetized plasma, through Faraday rotation and conversion. The combination of emission and propagation effects is complicated, so numerical radiative transfer methods are essential in understanding the polarization of M87* and Sgr A*.

CP structure can be used to understand the magnetic field structure of the accretion disk and field geometry of GRMHD models under certain conditions of observing angles and optical and Faraday thicknesses (Mościbrodzka et al. 2021; Ricarte et al. 2021; Tsunetoe et al. 2021). CP may also be a useful probe of plasma composition, since CP emission and Faraday rotation is sensitive to the electron–positron pair content (Wilson & Weiler 1997; Wardle et al. 1998; Homan et al. 2009; Anantua et al. 2020; Emami et al. 2021).

Unresolved CP measurements, particularly the handedness (or sign) of CP, have been hypothesized to indicate the sense of rotation of the disk (Enßlin 2003) or the magnetic field configuration: the structure and dipole moment of the magnetic field (Beckert & Falcke 2002). Constant handedness across long timescales indicates a constancy in either of these two properties. This is especially interesting in the case of Sgr A*, where the sign of CP has been observed to be constantly

negative across decades for 1.3 mm (and larger-wavelength) observations. In this paper, we investigate these hypotheses by comparing observational data at 1.3 mm to a library of simulated images. As we still do not have robust horizon-scale CP images of M87* and Sgr A*, it is useful to compare the integrated fractional CP values obtained from GRRT images to the ALMA data, to see which models are consistent.

The net CP is

$$v_{\text{net}} \equiv \frac{\int d^2x V(x, y)}{\int d^2x I(x, y)}, \quad (1)$$

where x, y are coordinates on the sky. Here I, V are the Stokes *I* and *V* images convolved with the beam. The net CP fraction is accessible from ALMA observations, with an effective beam size of $1'' \sim 10^5 GM/c^2$. The GRMHD model library reliably reproduces emission out to 200 μ as $\sim 40 GM/c^2$ diameter of the source, and to compare our simulations to observations, we assume that there is no significant emission between the two scales. In EHTC SgrA **II**, comparisons of horizon-scale baselines and short baselines such as ALMA-APEX (100 mas $\sim 2 \times 10^4 GM/c^2$) suggest that at least $\sim 90\%$ of the flux density (up to 100 mas) arises from the horizon-scale emission.

We will also occasionally refer to the average absolute CP fraction:

$$\langle |v| \rangle \equiv \frac{\int d^2x |V|}{\int d^2x I}. \quad (2)$$

Evidently, measurement of $\langle |v| \rangle$ requires a resolved image of the source and depends on the beam size.

The paper is organized as follows. In Section 2, we review the origin of CP in first-principles models in which the dominant emission mechanism is synchrotron emission from a relativistic thermal distribution of electrons. In Section 3, we describe the numerical models used in the analysis, along with the parameters that characterize the resulting model library. In Section 4, we investigate the CP properties of a single GRMHD model, highlighting properties that are generalizable across most of the library. In Section 5, we present the full library of v_{net} distributions, along with fits for their dependence on model parameters. Using unresolved very long baseline interferometry (VLBI) data of Sgr A* (Bower et al. 2018; Wielgus et al. 2022b), we attempt to constrain our models of Sgr A* in Section 6. In Section 7, we present a discussion on the models, including caveats, followed by a conclusion.

2. Physical Origins of CP

2.1. Polarized Radiative Transfer Equation

The time-independent radiative transfer equation, in flat space, along a ray labeled by s , in the Stokes basis (*I*, *Q*, *U*, *V*), is:

$$\frac{d}{ds} \begin{pmatrix} I \\ Q \\ U \\ V \end{pmatrix} = \begin{pmatrix} j_I \\ j_Q \\ j_U \\ j_V \end{pmatrix} - \begin{pmatrix} \alpha_I & \alpha_Q & \alpha_U & \alpha_V \\ \alpha_Q & \alpha_I & \rho_V & -\rho_U \\ \alpha_U & -\rho_V & \alpha_I & \rho_Q \\ \alpha_V & \rho_U & -\rho_Q & \alpha_I \end{pmatrix} \begin{pmatrix} I \\ Q \\ U \\ V \end{pmatrix}. \quad (3)$$

Here, j_S , α_S , and ρ_S are the emission, absorption, and Faraday rotation and conversion coefficients (“rotativities”) of component S of the Stokes vector. The coefficients depend on the

field strength and direction, the energy distribution function of particles (electrons for synchrotron radiation from an electron-ion plasma), and the frame in which they are measured. Scattering processes such as Compton scattering are negligible at millimeter wavelength for M87* and Sgr A* and have been neglected. CP is described by the V component of the Stokes vector. We follow the IEEE convention for definitions of the sign of CP, where $V > 0$ is right-handed CP, such that the electric field vector rotates in a right-hand direction, at a fixed point in space, with the thumb pointing along the direction of propagation (Hamaker & Bregman 1996).

Separating out the Stokes V equation,

$$\frac{d}{ds}V = j_V - \alpha_V I - \rho_U Q + \rho_Q U - \alpha_I V. \quad (4)$$

Evidently, Stokes V can be altered by direct, circularly polarized emission; polarization-specific absorption (i.e., the plasma acts as a circular polarizing filter); Faraday conversion from LP to circular; and polarization-nonspecific absorption. Polarization-nonspecific absorption α_I does not change the fractional CP V/I .

2.2. Origin of CP

In a spatially uniform magnetic field, the production of CP can occur in three ways, best seen in the radiative transfer Equation (3): intrinsic emission (j_V), selective absorption of CP ($\alpha_V I$), or Faraday conversion of linearly polarized into circular polarized light (ρ_Q and ρ_U components that interconvert U and Q , respectively, with V).

Using the radiative transfer equation in a homogeneous source (a “one-zone” model), one can estimate the LP and CP fractions of the emergent radiation (Jones & O’Dell 1977; Pandya et al. 2016). For parameters appropriate to EHT sources, a one-zone model produces an LP fraction that is large compared to the CP fraction, and the dominant production mechanism is Faraday conversion (see Figure 8 in EHTC M87 IX). The one-zone model overproduces both LP and CP, however—spatial inhomogeneities are important—and thus the case for Faraday conversion as the dominant source of CP in both simulations and observations cannot be made with one-zone models. We show, using an example model in Section 4.4, that although Faraday conversion is usually the dominant mechanism for the production of CP, intrinsic circularly polarized emission makes a non-negligible, and sometimes dominant, contribution.

2.3. Transfer Coefficients for Thermal Distribution

We adopt a thermal (Maxwell-Jüttner) electron energy distribution function. This is motivated by the notion that the EDF is likely to have an approximately thermal core extending up to Lorentz factor ~ 30 that produces millimeter emission (a hollow distribution, one in which $f(\mathbf{p})$ has a minimum at $\mathbf{p} = 0$, would be kinetically unstable; see Penrose 1960), and the idea that any superthermal tail on the distribution must not overproduce near-IR emission (Section 4.2.3 of EHTC SgrA V); i.e., the tail is constrained by the IR-to-millimeter color.

The emission coefficients are summarized in Dexter (2016), Pandya et al. (2016), and Marszewski et al. (2021); the absorption coefficients follow from Kirchoff’s law; and the Faraday coefficients ρ_S are given in Pandya et al. (2018).

It is helpful in understanding the symmetries of the transfer equations to write out the transfer coefficients explicitly in the frame of the plasma. As is conventional in this field, we work in a Stokes basis, where Stokes U corresponds to LP at $\pm 45^\circ$ to the projection of the magnetic field on the plane perpendicular to the wavevector. Then the emissivity fits are (following Dexter 2016):

$$j_I(\nu, \theta) = \frac{ne^2\nu}{2\sqrt{3}c\Theta_e^2} I_I(x), \quad (5)$$

$$j_Q(\nu, \theta) = \frac{ne^2\nu}{2\sqrt{3}c\Theta_e^2} I_Q(x), \quad (6)$$

$$j_U = 0, \quad (7)$$

and

$$j_V(\nu, \theta) = \frac{2ne^2\nu \cot(\theta)}{3\sqrt{3}c\Theta_e^2} I_V(x). \quad (8)$$

Here, n is the electron number density, $-e$ is the electron charge, ν is the photon frequency, θ is the angle between the wavevector and magnetic field (sometimes called the observer angle), c is the speed of light, $\Theta_e \equiv k_B T_e / (mc^2)$ is the dimensionless electron temperature, $x = \nu/\nu_c$ with $\nu_c = (3/2)\nu_B \sin(\theta)\Theta_e^2$, $\nu_B = e|B|/(2\pi mc)$ (the cyclotron frequency), and m is the electron mass. The I_S do not change sign under field reversal $\mathbf{B} \rightarrow -\mathbf{B}$.

The absorptivities can be found from Kirchoff’s law (B_ν is the blackbody function):

$$j_S = \alpha_S B_\nu. \quad (9)$$

The Faraday coefficients (fits) are:

$$\rho_Q = \frac{ne^2\nu_B^2 \sin^2 \theta}{mc\nu^3} f(X) \left[\frac{K_1(\Theta_e^{-1})}{K_2(\Theta_e^{-1})} + 6\Theta_e \right], \quad (10)$$

$$\rho_U = 0, \quad (11)$$

$$\rho_V = \frac{2ne^2\nu_B}{mc\nu^2} \frac{K_0(\Theta_e^{-1})}{K_2(\Theta_e^{-1})} \cos \theta g(X), \quad (12)$$

where

$$X = \left(\frac{3}{2\sqrt{2}} 10^{-3} \frac{\nu}{\nu_c} \right)^{-1/2}, \quad (13)$$

$$g(X) = 1 - 0.11 \ln(1 + 0.035X), \quad (14)$$

and K_0 , K_2 are modified Bessel functions of the second kind at orders 0 and 2, respectively. A field reversal transforms $\theta \rightarrow \pi - \theta$, which thus reverses the sign of j_V , α_V , and ρ_V .

In a field-aligned Stokes basis, $j_U = \alpha_U = \rho_U = 0$, and thus the Faraday conversion term in the transfer equation reduces to $+\rho_Q U$. Stokes U in the field-aligned Stokes basis is therefore required to produce Stokes V by Faraday conversion. The Stokes U transfer equation reduces in the field-aligned basis, for a uniform plasma, to $dU/ds = \rho_V Q - \alpha_I U - \rho_Q V$, so Stokes V can be produced by Faraday rotation of Stokes Q followed by Faraday conversion to Stokes V . We must add a term to the transfer equation, however, if we force the Stokes basis to be field aligned at each point on the ray. This term captures the effect of the rotation of the field through an angle ψ in the plane perpendicular to the line of sight, which interconverts Stokes Q and U , with $dU/ds = \dots + 2d\psi/ds Q$, $dQ/ds = \dots - 2d\psi/ds U$. Restated, emission of linearly polarized light elsewhere along

the line of sight produces Stokes U locally that can be Faraday-converted to Stokes V . In the end, Faraday conversion acts on linearly polarized light produced by some combination of Faraday rotation and field-line rotation (or “twist”). Ricarte et al. (2021) explore this effect in detail, along with the resulting properties of the magnetic field, which are apparent in Faraday-conversion-produced CP maps of GRMHD models.

2.4. Symmetries of the Coefficients and RTE

Below, we investigate the net CP associated with GRMHD models. The models are turbulent and the CP fluctuates in time. We are interested in the distribution of the net CP $f(v_{\text{net}})$ for a GRMHD model with fixed time-averaged millimeter-wavelength flux density, black hole spin, magnetization, inclination, and eDF parameters.

The GRMHD equations are invariant under magnetic field inversion $\mathbf{B} \rightarrow -\mathbf{B}$, but the radiative transfer equation is not, because some of the transfer coefficients depend on the sign of \mathbf{B} . To fully sample f , then, we ought to include field-inverted models. Here, we describe the symmetry of the transfer coefficients under field inversion and its effect on the solution to the transfer equation.

Under field inversion, the handedness of the electron orbits around the magnetic field lines changes sign: an electron that orbits clockwise on the sky moves counterclockwise after field inversion. This change in handedness flips the sign of CP for the emitted radiation. This implies that j_V and α_V change sign. In addition, ρ_V , the coefficient governing Faraday rotation, also reverses sign under field inversion (see Equations (5)–(12)). None of the other coefficients change sign.

For a single layer of plasma with a uniform magnetic field and no background radiation (the Stokes vector vanishes where the line of sight enters the plasma), we find, using the analytic solution of the radiative transfer equation (Landi Degl’Innocenti & Landi Degl’Innocenti 1985), that Stokes U changes sign when the field is inverted because the only source is Faraday rotation (ρ_V), which also changes sign. Similarly, Stokes V changes sign, since j_V and Faraday-rotation-generated Stokes U change sign, but ρ_Q does not (see Equation (4)). In sum, in the single-layer model, Stokes I and Q are invariant under field inversion and Stokes U and V change sign.

Any deviation from the single-layer model destroys the symmetry of the Stokes vector under field inversion. For example, polarized background radiation provides initial Stokes U that is symmetrically converted to Stokes V , but this is added to directly emitted circularly polarized radiation (j_V) that is antisymmetric. Multiple-layer models are not symmetric, since the Stokes Q generated in one layer (symmetric) gets rotated into Stokes U in the next layer, where it can be Faraday-converted (symmetric) to Stokes V , and this is added to the antisymmetric direct emission. We thus expect that the more complicated geometry of the GRMHD models will not obey a simple symmetry under field inversion. However, if the symmetric processes dominate over the antisymmetric processes (or vice versa), the v_{net} distributions could be approximately symmetric (or antisymmetric) to an inversion of \mathbf{B} . In Section 5, we see that some models flip in v_{net} with the inversion of \mathbf{B} , suggesting that intrinsic CP emission (j_V) or Faraday rotation followed by Faraday conversion ($\rho_Q \rho_V$) are dominant.

2.5. One-zone Model

We can crudely estimate the degree of CP expected in Sgr A* and M87* using a one-zone model. The model consists of a uniform sphere of hot plasma with radius $r = 5GM/c^2$. The uniform sphere has constant radiative transfer coefficients, the background radiation vanishes, and the spacetime is Minkowski.

The magnetic field strength and number density of the plasma can be estimated using the one-zone model, following EHTC M87 [V](#) and EHTC SgrA [V](#) for M87* and Sgr A*. As in those papers, we assume the electrons have a thermal (Maxwell–Jüttner) distribution function. The electron temperature and ion temperature need not be equal to each other, as the plasma is collisionless and there may be preferential heating of ions by turbulent dissipation (Quataert & Gruzinov 1999; Yuan & Narayan 2014; Ressler et al. 2015; Mościbrodzka et al. 2016; Zhdankin et al. 2021). We set the dimensionless electron temperature $\Theta_e \equiv kT_e/(m_e c^2) = 10$. The magnetic pressure $B^2/(8\pi)$ is set equal to the gas pressure, assuming the ion-to-electron temperature ratio is 3 and that the gas is pure hydrogen. The angle between the magnetic field and line of sight is set to 60°. The 1.3 mm flux density is set equal to the observed 0.7 Jy for M87* and 2.4 Jy for Sgr A*. Then the number density and magnetic field strength are

$$n_{e,\text{M87}*} = 3.3 \times 10^4 \text{ cm}^{-3}; B_{\text{M87}*} = 4.8 \text{ G}, \\ n_{e,\text{Sgr A}*} = 10^6 \text{ cm}^{-3}; B_{\text{Sgr A}*} = 29 \text{ G},$$

where we have iterated numerically over n_e to find a solution.

Given the density and magnetic field strength, we can compute the CP fraction using the exact solution to the polarized radiative transfer equation (Landi Degl’Innocenti & Landi Degl’Innocenti 1985; Mościbrodzka & Gammie 2018). We find

$$\text{CP}_{\text{M87}*} = 16.7\% \quad (15)$$

and

$$\text{CP}_{\text{Sgr A}*} = 5.1\%. \quad (16)$$

These CP values give an estimate of the resolved CP fractions ($\langle |v| \rangle$), which are consistent with the per-pixel CP fractions in simulations (see Figure 1, for example). In comparison, v_{net} observations (Table 1) and v_{net} in simulations are much lower (Figures 5 and 16), which suggests cancellations across different parts of the image.

In the vicinity of the one-zone model parameters, we can probe the effects of intrinsic emission and Faraday conversion on Stokes V . The optical and Faraday depths (α_{fr} , $\rho_{Q\text{fr}}$, and $\rho_{V\text{fr}}$) are approximately 0.4—in between optically/Faraday thin and thick. In the optically/Faraday-thin regime, Stokes V is well approximated by $j_{V\text{fr}}$. In the moderately optically thick regime, Faraday effects are dominant; the solution to Stokes V with $j_V = \alpha_V = 0$ is similar to the full solution. At longer wavelengths, absorption effects play an important role. Further analysis of CP versus frequency for the one-zone model is presented in Appendix A.

3. Numerical Model

3.1. GRMHD Models

We use a set of ideal GRMHD simulations for the KHARMA GRMHD simulation library in EHTC SgrA [V](#) (v3) and analyzed in detail in V. Dhruv et al. (2024, in

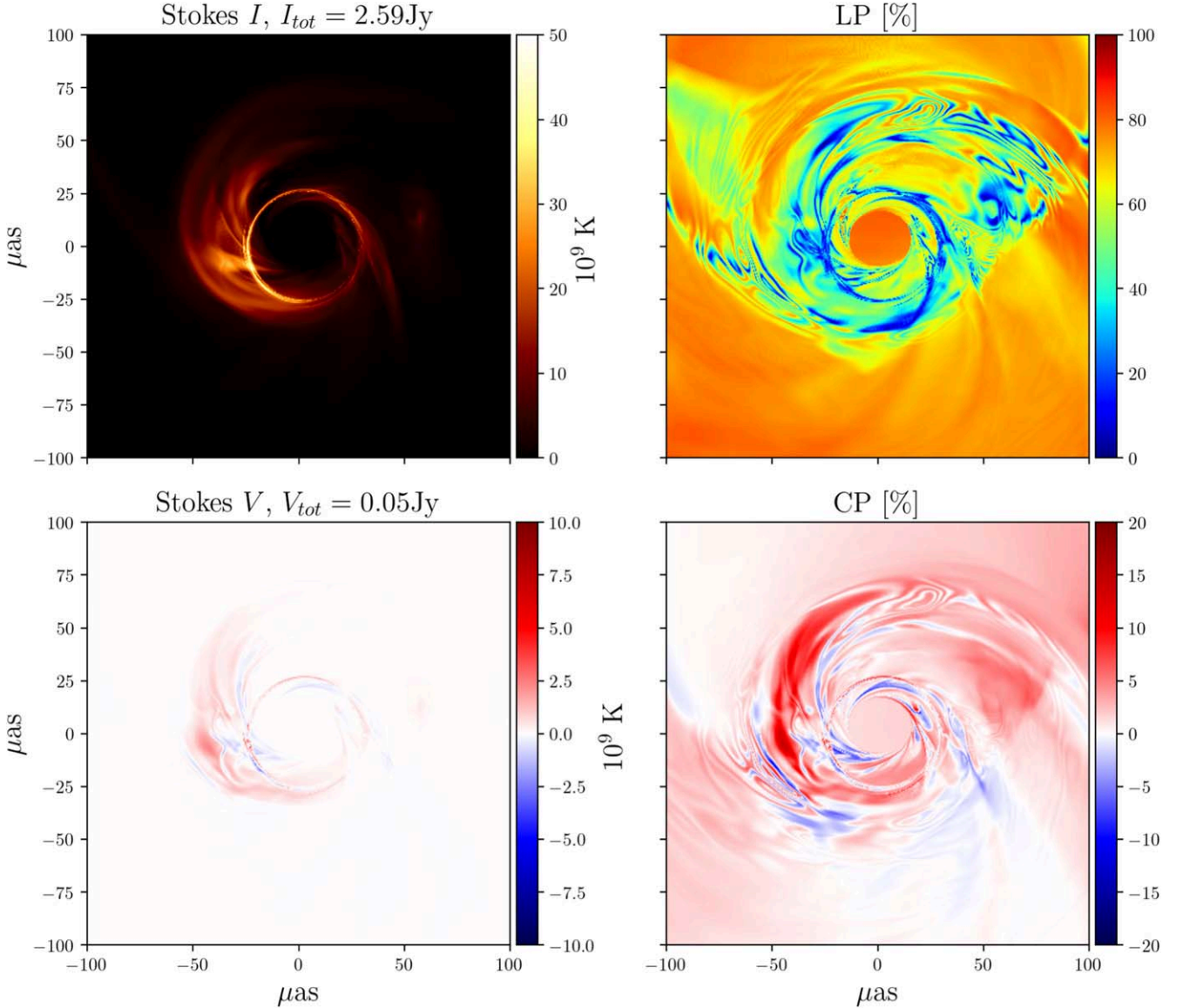


Figure 1. Sample MAD, spin = +0.5 at $2.75 \times 10^4 GM/c^3$, $R_{\text{high}} = 160$, and inclination 30° simulated Sgr A* image using `ipole`. The top and bottom left panels show the Stokes I and V maps, respectively, in brightness temperature units. The top and bottom right panels show the fractional LP and CP maps, respectively. The resolution is 0.5 μas per pixel.

preparation). The models are run using KHARMA¹¹ (Prather 2022, 2024) for $3 \times 10^4 GM/c^3$. The GRMHD model parameters are described in detail in Section 3.3. The GRMHD models are nonradiative and therefore invariant under rescaling of the density of the plasma. We choose a density scale (equivalently an accretion rate or mass unit \dot{M}) so that the simulation flux density matches the observed flux density.

3.2. Radiative Transfer Numerical Model

We image the GRMHD simulation snapshots using the GR ray-tracing code `ipole` (Mościbrodzka & Gammie 2018). The images are made by evaluating the intensity at a grid of points lying at the center of the image pixels in a fictitious camera. The photon trajectories are integrated backward from the

camera to, or past, the black hole. Then the radiative transfer equation is integrated forward along the geodesic to the camera, using the appropriate relativistic version of Equation (3) (Mościbrodzka & Gammie 2018).

3.3. Image Library Parameters

The library parameters include both GRMHD model parameters and GRRT model parameters. Our library has five parameters—two GRMHD and three GRRT:

1. The magnetic flux through one hemisphere of the hole Φ_{BH} , cast in dimensionless form $\phi \equiv \Phi_{\text{BH}}(\dot{M}(GM/c^2)^2c^{-1})^{-1/2}$. GRMHD models with $\phi \sim 1$ are known as Standard and Normal Evolution (SANE; Narayan et al. 2012; Sadowski et al. 2013). Models with $\phi \sim 15$ are known as MADs (Igumenshchev et al. 2003; Narayan et al. 2003). MAD and SANE models are obtained by manipulating the magnetic field in the initial conditions.

¹¹ KHARMA is a GPU-enabled, performance-portable version of HARM (Gammie et al. 2003). It is publicly available at <https://github.com/AFD-Illinois/kharma>.

Table 1
Measurements of CP Fraction at 1.3 mm for EHT Targets

Reference	Source	Mean v_{net} (%)	Epoch v_{net} (%)
Muñoz et al. (2012)	Sgr A*	-1.2 ± 0.3	-1.1
			-1.2
			-1.1
Bower et al. (2018)	Sgr A*	-1.1 ± 0.2	-1.3
			-0.9
			-1.3
Goddi et al. (2021)	Sgr A*	$[-1.0, -1.5] \pm 0.6$	N/A
Goddi et al. (2021)	M87*	$\lesssim \pm 0.8$	N/A
Wielgus et al. (2022b)	Sgr A*	-1.23 ± 0.4	-1.5
			-1.4
			-0.9
			-1.0
			-1.0

Note. Note that for Wielgus et al. (2022b), the epoch values are averages of 3 hr windows. While we report epoch values for Muñoz et al. (2012), we only use the ALMA epoch v_{net} for comparing our simulations with Sgr A*.

2. Black hole spin, a_* , with $a_* = -0.9375, -0.5, 0, 0.5$, and 0.9375 . Negative spin indicates that the accretion flow is retrograde.
3. The eDF parameter, R_{high} (Mościbrodzka et al. 2016), which sets the ion-to-electron temperature ratio $R = T_i/T_e = R_{\text{high}}\beta_p^2/(1 + \beta_p^2) + 1/(1 + \beta_p^2)$, where β_p is the ratio of the gas pressure to magnetic pressure. Typically, β_p is higher near the midplane than at the poles, so a high/low value of R_{high} implies less/more emission contribution from the midplane. We set $R_{\text{high}} = 1, 10, 20, 40, 80$, and 160 for M87* and $1, 10, 40$, and 160 for Sgr A*.
4. Inclination, θ , which is the angle between the wavevector and the orbital angular momentum of the accretion flow. The inclination is $10^\circ, 30^\circ, 50^\circ, 70^\circ, 90^\circ, 110^\circ, 130^\circ, 150^\circ$, and 170° for Sgr A*. In models with $\theta < 90^\circ$ ($\theta > 90^\circ$), the accretion disk rotates counterclockwise (clockwise) on the sky. For M87*, the black hole is imaged at an inclination of 17° for a negative spin and 163° for a non-negative spin, so that the inclination is chosen to match the large-scale jet and the image asymmetry is chosen to match EHT images (see EHTC M87 V).
5. The sign of the magnetic field. The field can be inverted without changing the GRMHD solution, so we have re-imaged all models with a reversed field. We will use “aligned field” to refer to models with a field near the poles that is parallel to the accretion flow orbital angular momentum, and “reversed field” to refer to models with polar fields that are antiparallel to the accretion flow orbital angular momentum.

Each model contains 600 images evenly spaced in the interval $15,000$ – $30,000$ GM/c^3 (1 GM/c^3 is 3×10^5 and 20 s for the M87* and Sgr A* parameters, respectively). The interval is chosen so that fluctuations associated with the initial conditions have damped away and the accretion rate is stable. The density scale \mathcal{M} is fit every 5000 GM/c^3 to account for any potential depletion of mass in the accretion disk. For M87*

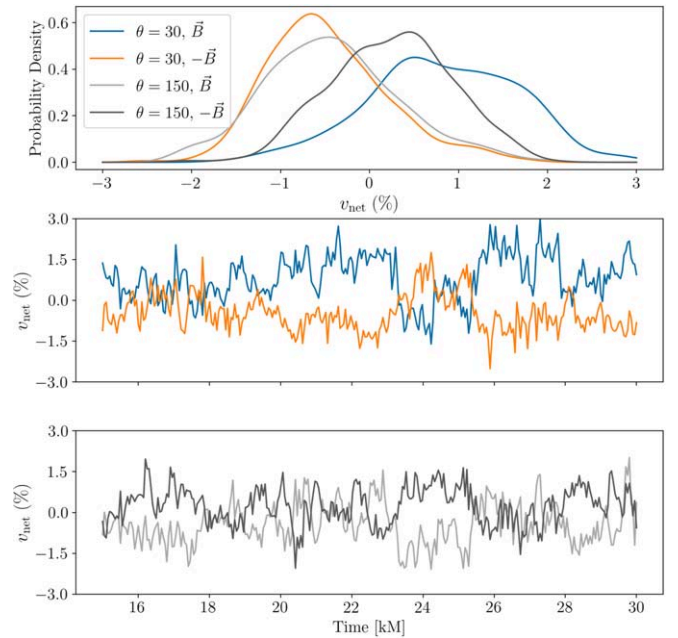


Figure 2. v_{net} for an Sgr A*, MAD, spin $+0.5$, $R_{\text{high}} 160$, and inclination 30° (and 150°) model for both aligned- and reversed-field configurations. Top plot: kernel density estimates of the distributions using kernel widths of 0.3% to match the observational errors in Bower et al. (2018). Bottom two plots: v_{net} light curves across $15,000 GM/c^3$ for each of these distributions, with colors matching the legend above. The mean of the distributions is parameterized by $(\theta, \pm B)$: $(30^\circ, B) = 0.83\%$, $(30^\circ, -B) = -0.47\%$, $(150^\circ, B) = -0.42\%$, $(150^\circ, -B) = 0.25\%$.

and Sgr A*, the average flux is within 5% of 0.7 Jy and 2.4 Jy, respectively (EHTC M87 IV; Wielgus et al. 2022a).

4. CP for a Fiducial Model

First, consider a single, fiducial model: a MAD, spin $+0.5$, $R_{\text{high}} 160$, and inclination 30° (and 150°) model for Sgr A*. This is one of the best-fit models, based on EHT and multiwavelength constraints (EHTC SgrA V).

4.1. Sample Image

Figure 1 shows a snapshot of Stokes I , Stokes V , the LP fraction, and the CP fraction. One key feature of the image, typical of most of the models, is positive and negative fluctuations in CP that cancel out when v_{net} is evaluated. In the image, the CP fraction in individual pixels is as large as 10%–15%, but integration over the image reduces the net CP fraction to 1%.

4.2. CP Distribution

The CP fluctuates in time. To test a model, we compare the model’s distribution of CP to the observed distribution of CP. The top panel in Figure 2 shows the distribution of CP broken down into the aligned- and reversed-field models, as well as the distribution seen from above (inclination 30°) and below (inclination 150°). The time evolution is shown in the bottom two panels for each subset of the model. Evidently, reversing the field, or imaging from a complementary inclination, does not flip the distribution about 0, consistent with the discussion above; however, there appears to be some anticorrelation with reversing the field, which suggests intrinsic CP emission or Faraday rotation being important for v_{net} in these models.

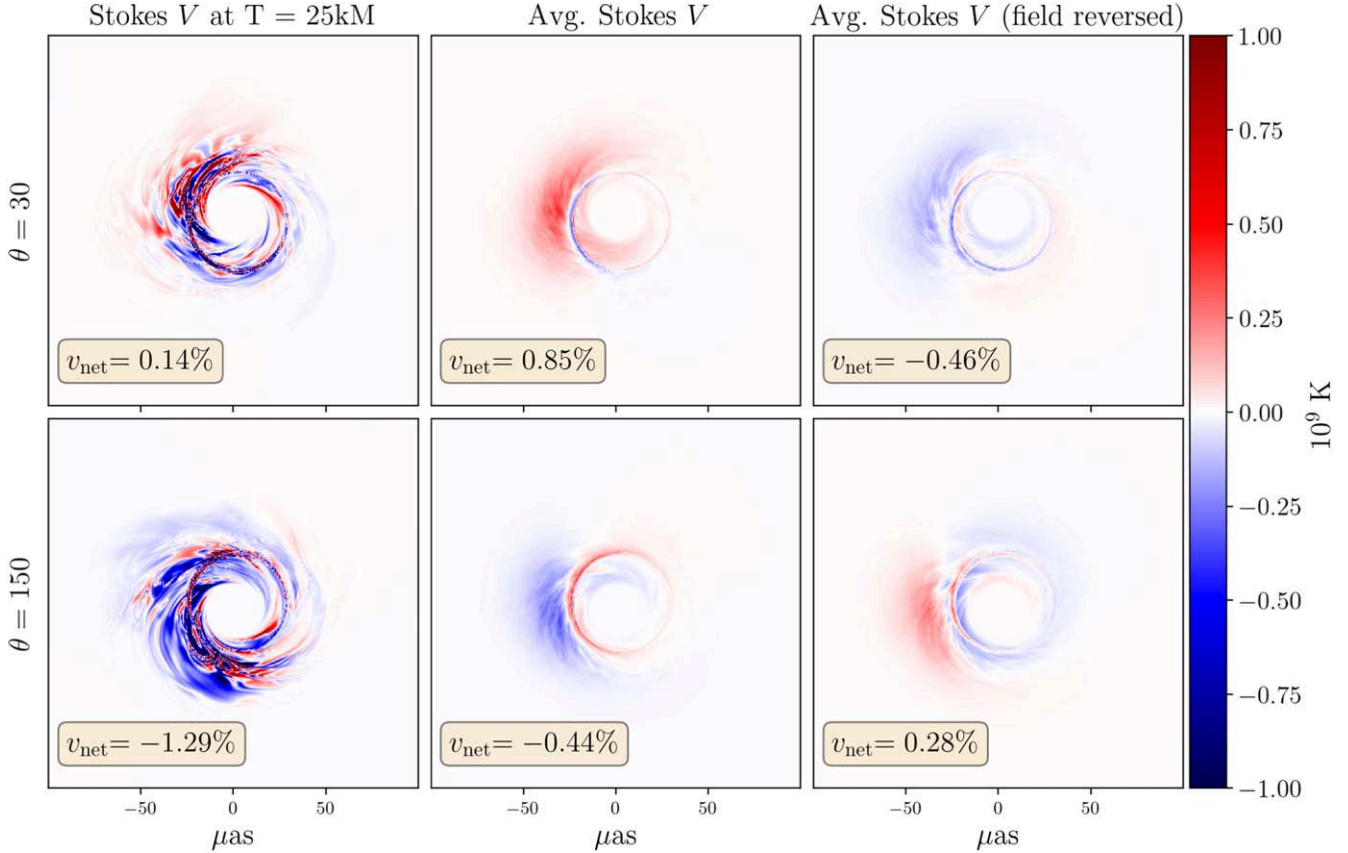


Figure 3. Snapshots and average images of Stokes V (in brightness temperature) for an Sgr A* MAD, spin $+0.5$, $R_{\text{high}} = 160$, and inclination 30° (and 150°) model for both aligned- and reversed-field configurations.

Notice that CP changes sign as a result of the fluctuations in the small patches of polarization seen in Figure 1.

4.3. Average Images

Time-averaged images provide information about which CP generation mechanism dominates. The mean of the distribution of the integrated CP fraction is not precisely equivalent to the integrated CP fraction of a time-averaged image, but if the total flux of each image is close to the mean value of 2.4 Jy, then the two quantities are comparable. Figure 3 shows the average images for the fiducial model.

For this particular model, after averaging, the region that dominates the CP map is emission near the disk, close to the black hole (EHTC M87 V). The bright positive feature is the region of the accretion disk where the fluid velocity is aligned with the line of sight, and thus it appears prominently due to Doppler boosting. A clear ring-like structure is seen. Its opposite sign is a consequence of the relatively low Faraday rotation thickness of the image and the imprint of the magnetic fields on Stokes V through Faraday conversion, as observed in Mościbrodzka et al. (2021) and Ricarte et al. (2021). The latter paper, in particular, shows that the sign of CP in the lensed photon ring always has the opposite sign of CP arising from Faraday conversion in Faraday-thin images.

4.4. Contribution of Transfer Coefficients

Here, we probe the relative importance of processes contributing to the net CP by turning off individual radiative transfer coefficients one by one. We re-image the fiducial

model with 30 snapshots across 15,000M, turning off j_V (intrinsic CP emission), α_V (CP absorption), ρ_Q (Faraday conversion), and ρ_V (Faraday rotation). Figure 4 shows time series of CP in each case.

Evidently, CP-selective absorption of unpolarized radiation (α_V) plays a negligible role. This is because α_V is calculated from the Planck function, j_V is about 2 orders of magnitude smaller than j_i , and the models are optically thin. The remaining three coefficients all affect $\langle |v| \rangle$, with ρ_Q being the dominant mechanism of CP production, as $\langle |v| \rangle$ is highly suppressed when excluding Faraday conversion. Although j_V is subdominant, it is non-negligible. This is also observed in MAD model images for M87 at different R_{high} values, where we see the inclusion of j_V can increase $\langle |v| \rangle$ by as much as 50%. Faraday conversion and intrinsic CP emission both contribute to $\langle |v| \rangle$, but the effect of Faraday rotation varies. The importance of each coefficient also varies in time. We conclude that only α_V is negligible, but all remaining effects need to be accounted for to accurately model CP.

A large number of models were investigated in a similar manner in EHTC M87 IX, with one snapshot from each model that passed all polarimetric constraints, testing the relative effects of j_V , ρ_V , and ρ_Q . While the definitions of $\langle |v| \rangle$ in this paper, and $\langle |v| \rangle$ in EHTC M87 IX, differ by a Gaussian blur of 20 μas in the latter, the results are consistent, in that the contribution of j_V is subdominant compared to ρ_Q .

The optical depths, magnetic field strength, and thus CP production mechanisms vary greatly across models. Combined with the nontrivial effect of including the reversed-field distributions, it is not possible to formulate a universally applicable,

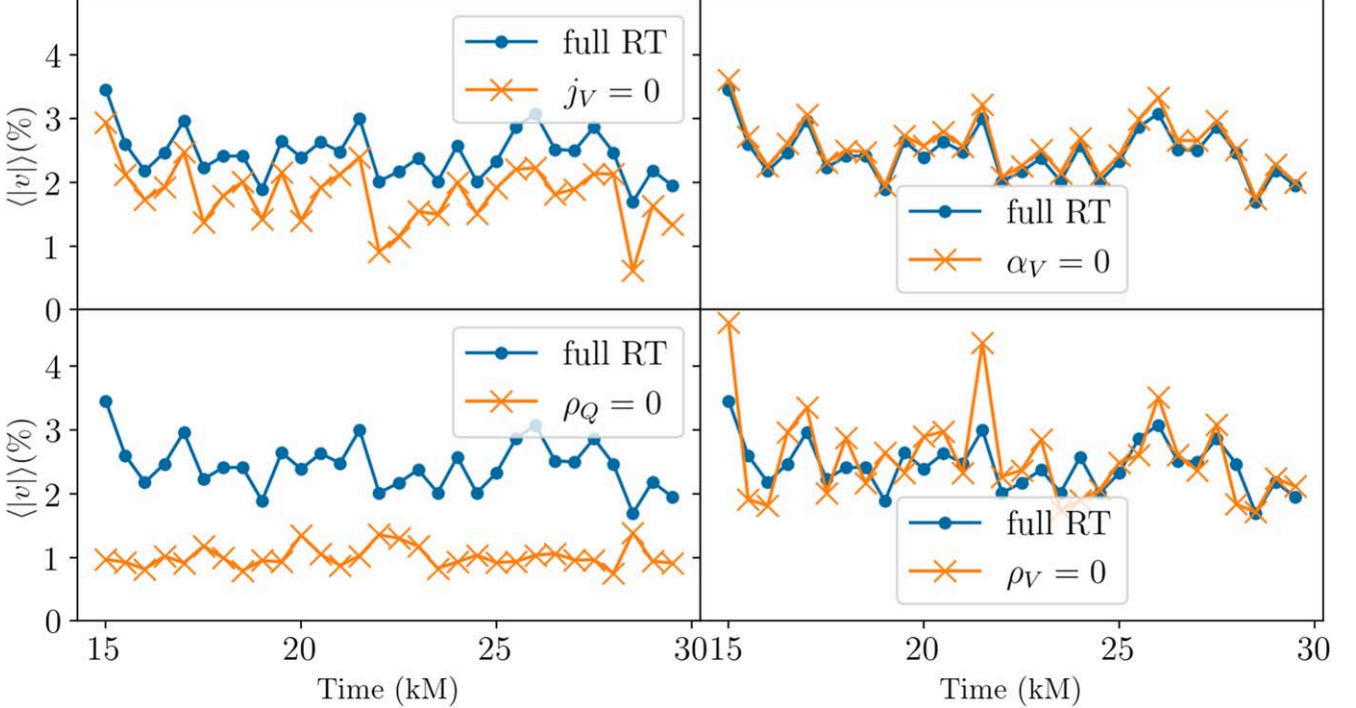


Figure 4. Comparison of $\langle |v| \rangle$ (resolved CP fraction) for a MAD, spin $+0.5$, $R_{\text{high}} = 160$, and inclination 30° model across $15,000\text{M}$ by re-imaging the model, setting each coefficient to 0. The subplots each probe the effect of a process that influences CP, in clockwise order from top left: j_V (intrinsic CP emission), α_V (CP absorption), ρ_V (Faraday rotation), and ρ_Q (Faraday conversion).

simple model for CP that is valid across all parameters. By comparing the aligned- and reversed-field distributions, however, we can understand whether each model’s CP is produced via **B** field-polarity-invariant pathways (Faraday conversion through field twist) or noninvariant pathways (intrinsic emission or Faraday conversion through Faraday rotation).

5. CP Distributions across All Models

Convergence tests of distributions of v_{net} are given in Appendix B—the v_{net} distributions appear converged with respect to GRMHD resolution and GRRT image resolution. Figures 5–6 show the v_{net} distributions (aligned- and reversed-field) of Sgr A* for all models in the library. M87* distributions are given in Appendix C. The first and second moments of each distribution are given in Appendix D.

Comparing the MAD and SANE models, we see that the SANE models have higher v_{net} , particularly for lower- R_{high} values. For the MAD models, almost all models have $|v_{\text{net}}| < 2\%$, whereas the SANE models have snapshots with $|v_{\text{net}}| > 4\%$. Given the low detected values of CP for Sgr A* and M87*, some of our SANE models can be ruled out. The MAD models also exhibit cleaner trends across model parameters, whereas the SANE (especially low- R_{high}) models are more turbulent. Ricarte et al. (2021; see Figures 8, 9, and 13) also find that SANE models have higher Faraday depths than MADs. Higher Faraday depth implies more scrambling of LP, and thus, to the extent that Faraday conversion is important, scrambling of CP. This scrambling hides imprints of the magnetic field in CP measurements of SANEs compared to MADs.

The effect of field reversal is mixed. For some SANE models, v_{net} is nearly antisymmetric (spin 0, $R_{\text{high}} = 10$), while for a few models v_{net} is nearly symmetric (spin 0, $R_{\text{high}} = 1$). A

majority of the SANE models, and all of the MAD models, show imperfect symmetry/antisymmetry under field reversal, indicating that both magnetic field twist and Faraday rotation + intrinsic emission contribute significantly.

In Sgr A*, CP is almost 0 for edge-on models. This can be attributed to the cancellation that occurs across every image due to symmetries in the magnetic field geometry (see Ricarte et al. 2021; Tsunetoe et al. 2021 for detailed descriptions). Edge-on models tend to have higher Faraday depths, which also contribute to the increased cancellation of CP across the image. We find that the Faraday rotation depths for SANE models are 2 orders of magnitude higher than for the corresponding MAD models. Faraday depth is a strong function of R_{high} (increases), spin (decreases from retrograde to prograde), and inclination (increases until 90°). R_{high} and spin directly influence the temperature of the electrons, and models with hotter electrons have lower Faraday depths.

5.1. Parameter Dependence of CP Distributions

Here, we focus on parameters that can influence v_{net} across all models, such as spin, inclination, R_{high} , and frequency.

5.1.1. Spin Dependence

The black hole spin influences the sign and shape of the v_{net} distributions. Prograde spin model snapshots contain components with opposite signs of v_{net} , i.e., more spatial cancellation than in low-spin models. As a result, high-spin prograde model distributions of v_{net} are broader than low-spin models.

An image in Stokes I (or V) can be divided into the weakly lensed component ($n = 0$) and a strongly lensed component, where photons wrap around the black hole in n half circles ($n = 1, 2, 3, \dots$; see Johnson et al. 2020). Each ring n is

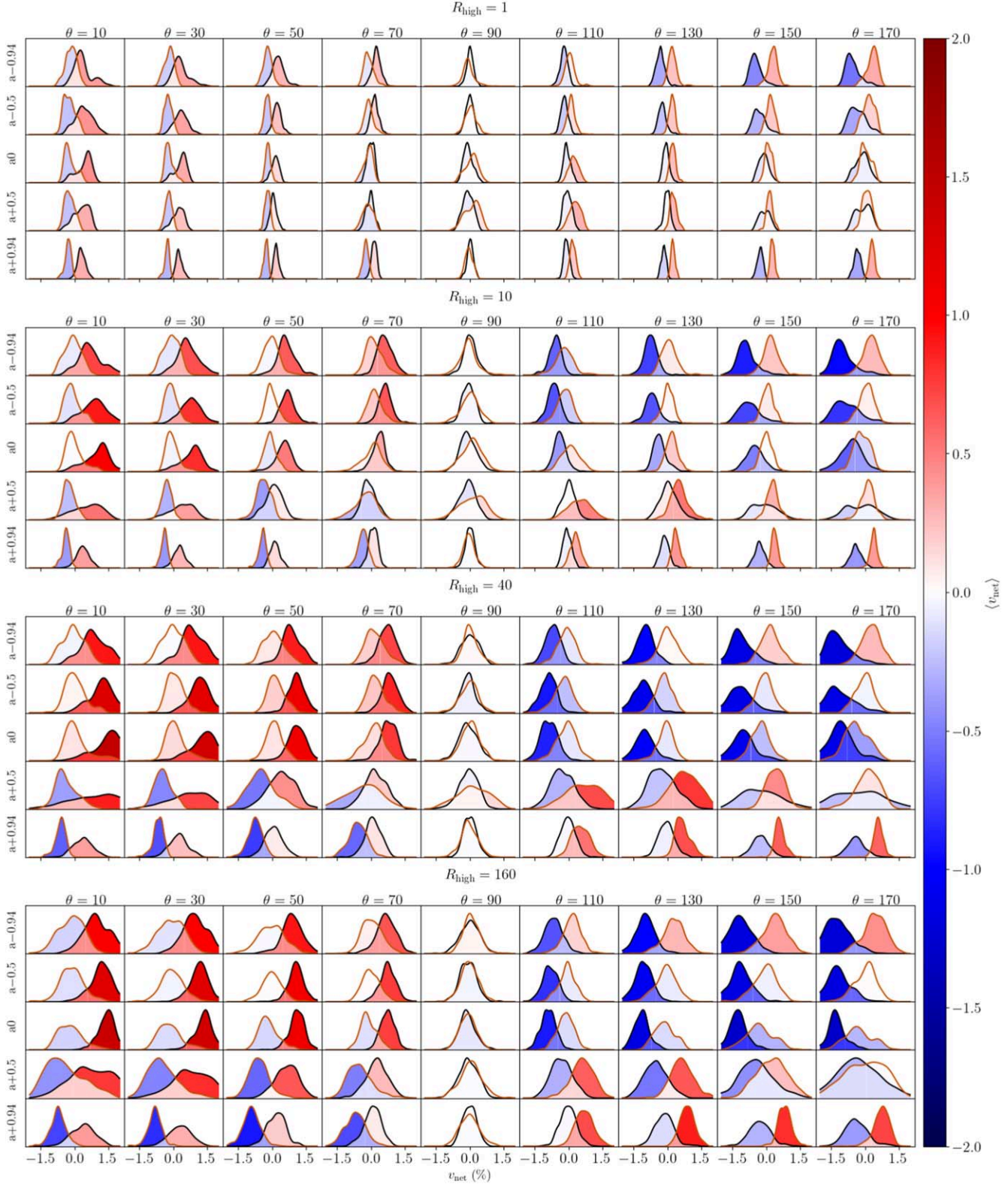


Figure 5. Distributions of v_{net} for all the MAD Sgr A* models. For each subplot, the x -axis corresponds to v_{net} and the y -axis corresponds to the probability density function of the model. Across the subplots, the y -axis spans spin, grouped in R_{high} . The x -axis spans observer inclination. The black (orange) lines represent the aligned- (reversed-) field distributions, respectively. The color filled within the distributions corresponds to the mean v_{net} and the color in the overlapping region shows the mean v_{net} of both field configurations combined. The height of each subplot is adjusted, so that the maximum of the distribution has the same height in all panels.

$\sim \exp(-\pi)$ fainter than the next. In this work, we see effects primarily from the $n = 0$ and $n = 1$ images.

For face-on prograde MAD models, the opposite-signed $n = 0$ and $n = 1$ portions of the image become important, with

the $n = 1$ ring becoming the dominant source of fractional CP, as seen in Figure 7, which shows average images of CP for a MAD model across spin. The $n = 0$ mode of the CP image has contributions from intrinsic emission and Faraday conversion,

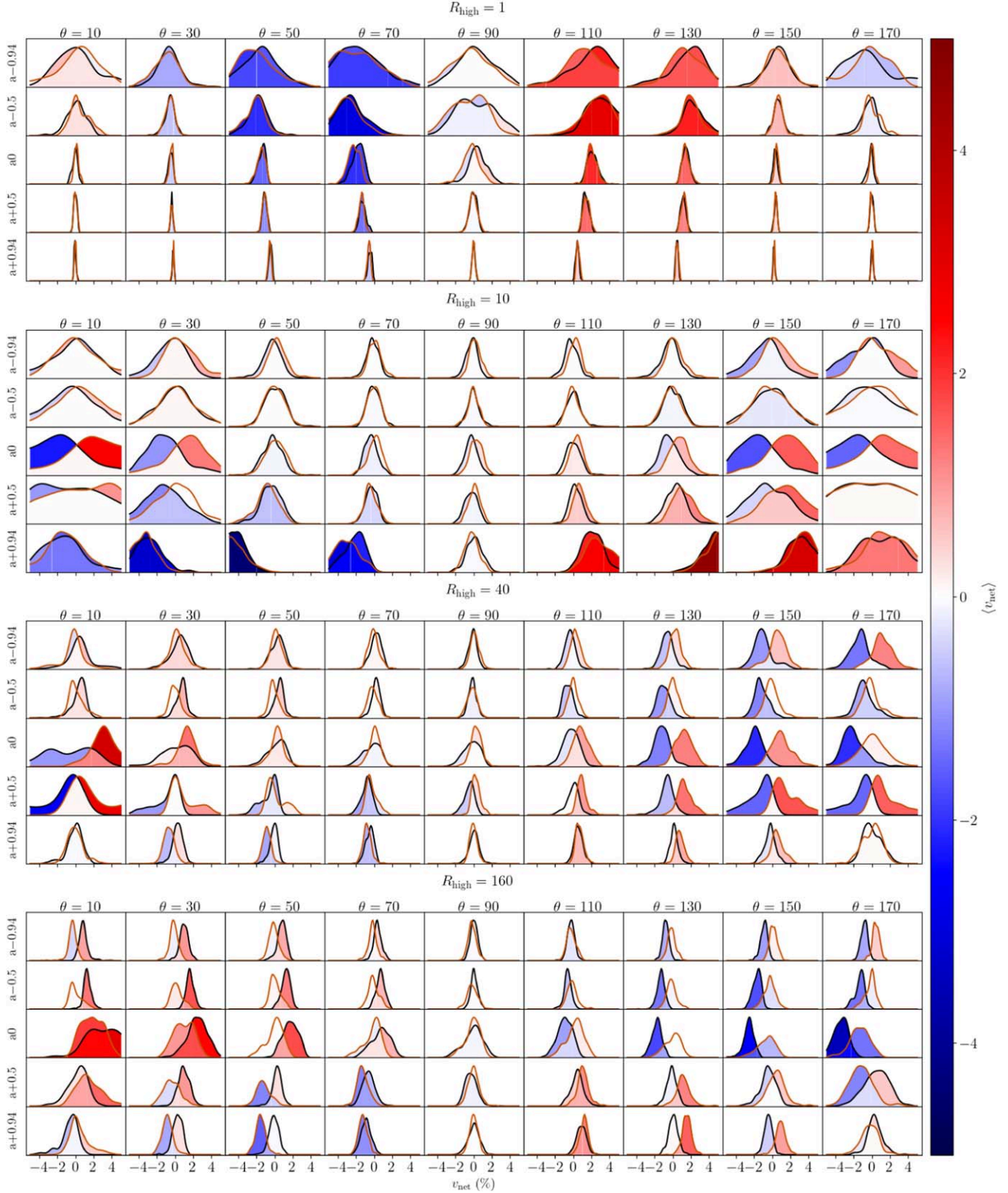


Figure 6. The same as Figure 5, except for SANE distributions.

both through Faraday rotation and twist. In the Faraday-thin and optically thin regions with toroidal magnetic fields, the $n = 1$ photon ring is the opposite sign of the $n = 0$ component. The opposite sign of the photon ring is a consequence of Faraday conversion through the twist of the magnetic field, as

explored in Ricarte et al. (2021). The field structure of retrograde models is less toroidal and thus the $n = 1$ contribution is reduced. This effect is also reduced as the Faraday thickness increases and thus is less prominent in retrograde and SANE models. While the sign flip in the $n = 1$

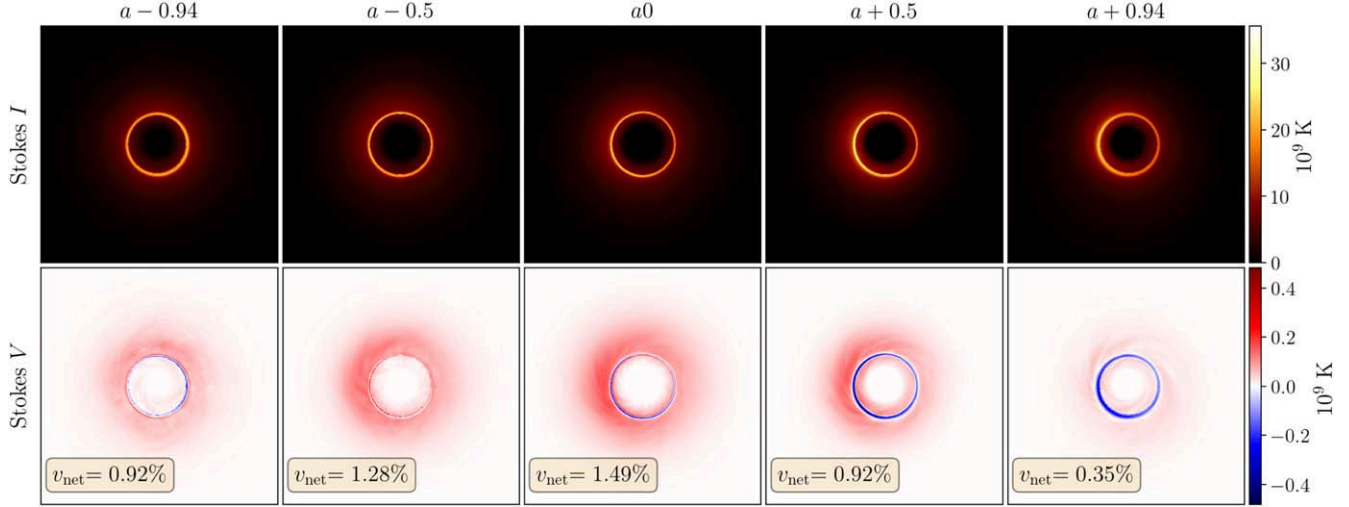


Figure 7. Average images of Stokes I and V across spin for Sgr A* MAD models at $R_{\text{high}} = 40$, inclination 10° .

photon ring is prominent at face-on inclinations, this effect of prograde models having opposite-signed v_{net} distributions is also seen at higher inclinations, although it is uncertain if the same phenomenon is responsible. It is possible that as the spin increases, the contribution of the $n=0$ portion of the image decreases, but further investigation would be necessary.

5.1.2. Inclination Dependence

Images at observer inclination $\theta \neq 90^\circ$ typically contain contributions from the near- and farside regions ($z > 0$ and $z < 0$, where $z = 0$ is the midplane of the system). For both of these regions, $\mathbf{k} \cdot \mathbf{B}$ is important, along with the direction of twist of \mathbf{B} along the geodesic. At low inclinations, photons from the farside region have larger optical and Faraday depths, from gravitational lensing increasing the path length. For higher- R_{high} models, the cool disk may also increase the Faraday depth for farside photons traveling through it. As a result, the farside contribution can be scrambled or even change sign in certain regions, but it is unlikely to exactly cancel out, or surpass, the nearside component, thus generating a net v_{net} biased toward the near-field component.

For inclinations $\theta < 90^\circ$ and aligned magnetic fields, MAD models on average have positive v_{net} (ignoring photon ring effects). In the nearside region, $\mathbf{k} \cdot \mathbf{B} > 0$, so $j_V > 0$ and $\rho_V > 0$. For Faraday-thin regions, $\rho_V > 0$ increases Stokes U , which in turn increases Stokes V via conversion (see Equation (3)). Faraday conversion through the twist in magnetic fields also contributes toward $v_{\text{net}} > 0$; Ricarte et al. (2021) demonstrate this for a face-on model by considering the twist of \mathbf{B} along the jet as it (the jet) broadens out (denoted as the vertical twist ξ_V). The vertical twist ξ_V (and the Stokes basis rotation) is clockwise along the line of sight, which corresponds to a rotation of $Q > 0$ to $U > 0$ and thus $V > 0$ as $\rho_Q > 0$. Another form of twist explored in Enßlin (2003) and Ricarte et al. (2021), the transverse twist (ξ_T), occurs for edge-on models. For disks rotating counterclockwise in the sky ($\theta < 90^\circ$), trailing magnetic fields embedded in the disk will be twisted counterclockwise along the line of sight (for the approaching jet), leading to $V < 0$. As this effect is maximal for edge-on simulations, its imprint on inclination compared to that of the vertical twist is minimal.

While it is difficult to ascertain the sense of twist of \mathbf{B} for intermediate observer inclinations, one can expect the effect of twist along the jet to reduce as the observer inclination increases. Due to symmetries in the global magnetic field across the midplane, as $\theta \rightarrow 90^\circ$, any additional effects of twist should cancel out. Also, a complementary inclination angle will reverse $\mathbf{k} \cdot \mathbf{B}$ and the twist of \mathbf{B} , thus reversing the sign of CP. Thus, on average, the v_{net} distributions should follow a cosine function, but fluctuations will prevent individual snapshots from following a neat pattern.

From Figures 5 and 6, we see that this is the case for the aligned- and reversed-field models. The universality of this behavior across all models suggests that the mean across field configurations encodes the sense of twist of the magnetic field, since CP generated from the conversion of LP via a twisted magnetic field is the only mechanism invariant to the sign of \mathbf{B} .

A mean positive v_{net} thus implies an overall clockwise twist in \mathbf{B} along \mathbf{k} for both retrograde and nonspinning models with $\theta < 90^\circ$ (where the $n=0$ contribution is dominant). It could also imply an overall counterclockwise twist for prograde models with $\theta > 90^\circ$, only in cases where the $n=1$ contribution is greater than the $n=0$ component, which is most $a+0.94$ models and a few $a+0.5$ models.

A mean negative v_{net} implies the same, but with the corresponding opposite sense of twist and observer inclinations. Thus, we find that the sign of the mean v_{net} is sensitive to not only the global sign of the magnetic field, but also the sense of rotation of the accretion flow.

5.1.3. R_{high} Dependence

As mentioned in Section 3.3, a higher R_{high} implies cooler electrons in the disk. This causes less emission from the midplane of the disk. For higher R_{high} , a higher mass unit (\mathcal{M}) is required to obtain the same output flux as that from a lower- R_{high} -value simulation, and this implies higher density and therefore an increase in all the radiative transfer coefficients. This causes two important effects. One is an increase in CP for individual pixels, because of increased Faraday conversion and emission. The other is a decrease in the overall CP, arising from an increase in depolarization: scrambled LP from Faraday rotation leads to scrambled CP through Faraday conversion. The presence of a cooler, denser

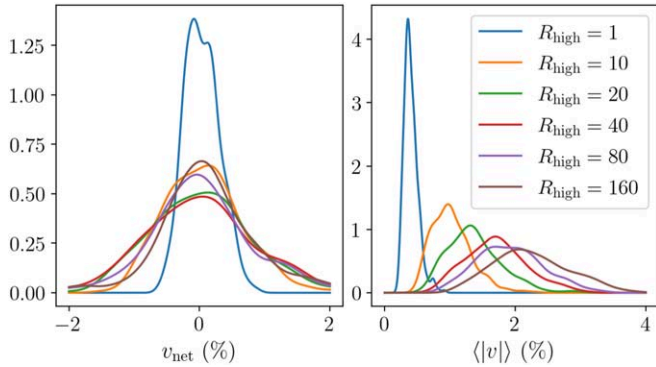


Figure 8. Kernel density estimations of the v_{net} and $\langle |v| \rangle$ distributions for a MAD, spin $+0.5$, M87* black hole for different R_{high} values. While there is no observable trend for v_{net} , there is a clear increase in $\langle |v| \rangle$ with R_{high} .

population of electrons in the disk midplane is particularly important for increasing Faraday rotation.

The overall effect is that v_{net} (unresolved CP) distributions broaden with increasing R_{high} , and $\langle |v| \rangle$ (resolved CP) distributions increase in magnitude with R_{high} . The distributions of v_{net} and $\langle |v| \rangle$ for different values of the R_{high} and M87* parameters are given in Figure 8. Although it is difficult to observe any trend in v_{net} (likely due to cancellations), a clear increase in $\langle |v| \rangle$ with R_{high} is seen. As this effect is seen for most spins, we conclude that resolved observations of Stokes V ($\langle |v| \rangle$) in the future can constrain electron temperature models. This is consistent with the results found in Mościbrodzka et al. (2021).

Models with $R_{\text{high}} = 1$ are qualitatively different in v_{net} , especially in the SANE models, as these models have hot, dense disks that dominate the emission in a relatively concentrated region (in the poloidal direction) in the midplane. Higher- R_{high} models, in comparison, require a higher scaling factor to obtain the same flux. This causes more contributions from both near and far jet-sheath regions, which combined with a cooler midplane can increase the Faraday depths and emission regions.

5.1.4. Frequency Dependence

While not a parameter explored in the image library, we investigate v_{net} of a few models versus frequency, shown in Figure 9 for three models: (MAD $a+0.5$, $R_{\text{high}} 160$, inclination 30°), (MAD $a+0.94$, $R_{\text{high}} 1$, inclination 30°), and (SANE, $a0$, $R_{\text{high}} 40$, inclination 130°). We find three different spectral behaviors of Stokes V , which suggest that different mechanisms are dominant in each model. The SANE model, while optically thin, remains Faraday-thick. Thus, even at higher frequencies, when probing inner regions of the accretion flow, the Stokes V signal does not significantly decrease. The MAD models are Faraday-thin near 230 GHz, so Stokes V reduces as frequency increases and the $R_{\text{high}} = 160$ model decreases faster compared to the $R_{\text{high}} = 1$ model. From the distributions of v_{net} , we find that the MAD $R_{\text{high}} 160$ model does not neatly change sign with \mathbf{B} reversal, whereas the $R_{\text{high}} 40$ model does. This suggests that Faraday conversion (through twisted magnetic fields) is important to the former (high- R_{high} model), but not the latter (lower R_{high}), where intrinsic emission or Faraday conversion through rotation dominate.

In Appendix A, we analyze the analytic solution to Stokes V for a single geodesic and find that Stokes V from just Faraday conversion decreases much faster with increasing frequency than Stokes V from intrinsic emission. Qualitatively, comparing

these analytic results (Figure 13 in Appendix A) to the numerical models (Figure 9) suggests that a steep ν^{-2} scaling in Stokes V , as seen in the MAD $a+0.5$, $R_{\text{high}} 160$ model, points to a Faraday-conversion-dominated model and a slow ν^{-1} scaling, as seen in the MAD $a+0.94$, $R_{\text{high}} 1$ model, is intrinsic-emission-dominated. The frequency scaling estimates are heuristic and an extensive frequency analysis across all models is needed for direct comparison with observations.

5.2. Fits to v_{net} Distributions

The mean and standard deviations of all v_{net} distributions are provided in Appendix D. Likely because of the mix of physical processes that contribute to CP, it is difficult to provide a simple fit to these moments that covers the entire model space. The Sgr A* MAD models, however, exhibit clear trends. The mean is readily fit by

$$\langle v_{\text{net}} \rangle = 0.61\% \cos(\theta) \left(1 - \frac{0.64}{R_{\text{high}}} \right) \left(S - \frac{(1+a)^2}{3} + 1 \right), \quad (17)$$

which we extracted using the PySR symbolic regression code (Cranmer 2020; Cranmer et al. 2020). Here, θ is the observer inclination and S is the sense of the magnetic field (1 for aligned and -1 for reversed cases). The fitting function recovers a cosine dependence on the observer inclination, which we attribute to the overall switch in sign from viewing at opposite poles, and increasing cancellations when observing edge-on, due to the symmetries of the magnetic field.

The mean v_{net} and the fit (Equation 17) are shown in Figure 10. The fit accurately measures the mean v_{net} of roughly 80% of the models to within 0.3% (absolute difference). The fits for the means and standard deviations of the SANE models do not permit such an accurate fit, but the raw data are provided in Appendix D.

6. Comparison to Observational Data

6.1. Sgr A*

Which models produce CP that matches Sgr A* and M87*? The detections and limits of v_{net} for M87* and Sgr A* are given in Table 1. For Sgr A*, the observations from ALMA given in Bower et al. (2018) and Wielgus et al. (2022b) are used as a constraint on the CP (8 data points, assumed to be uncorrelated, ranging from -1.5% to -0.92%). To test the models, a procedure similar to that in EHTC SgrA V is used. Two-sided K-S test p -values (p) are computed between distributions of the model and observations. The model is sampled every 400M to obtain an approximately uncorrelated sample. The model fails the constraint if both the aligned- and reversed-field distribution give $p < 0.01$, giving 99% confidence in rejecting the null hypothesis that the model and observations arose from the same distribution. The constraint plots are shown in Figure 11.

We have $27/180 = 15\%$ of the MAD models pass and $43/180 = 24\%$ of the SANE models pass the CP constraint. The SANE models are less constrained overall than the MAD models. This can be attributed to the higher fractional CP generated in general, increasing the chance that one combination of flow orientation and field configuration will produce sufficiently negative CP to pass the constraint.

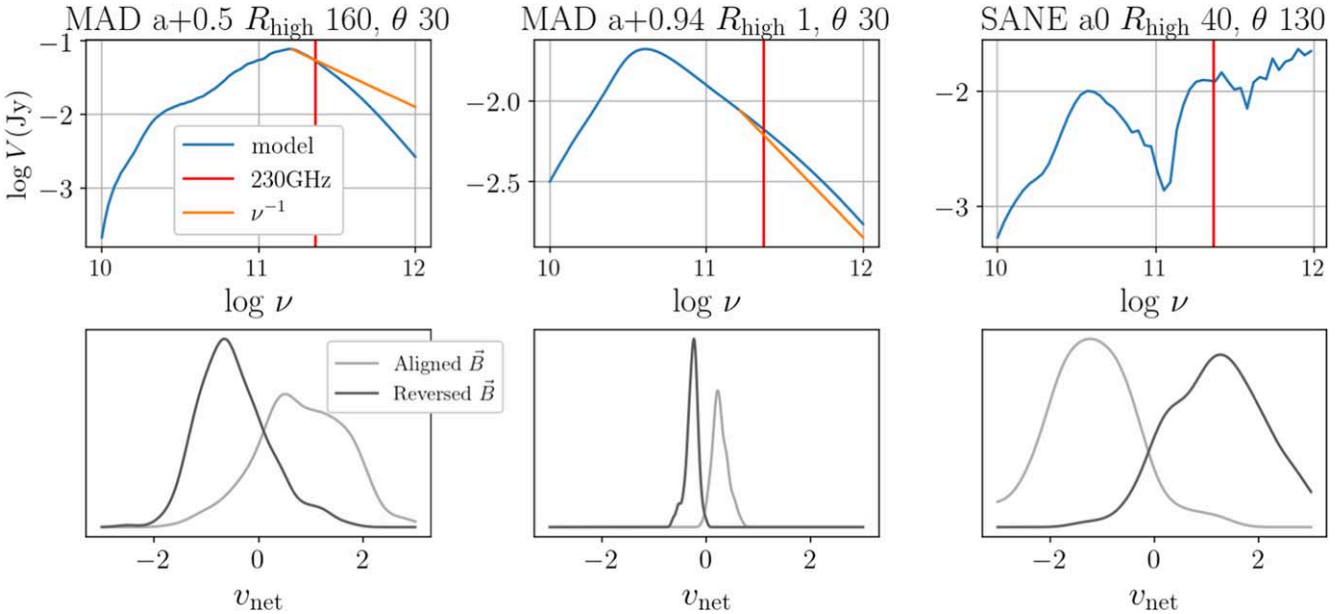


Figure 9. Upper row: image-integrated Stokes V for three different GRMHD models across frequency. ν^{-1} is plotted for comparison in the Faraday-thin regime. The red line indicates 230 GHz (1.3 mm), the frequency at which the model library is generated. Bottom row: distributions of v_{net} in time for both field configurations of the corresponding models at 230 GHz. The behavior of v_{net} with an inversion of field can inform the dominant CP mechanism that affects the spectral behavior.

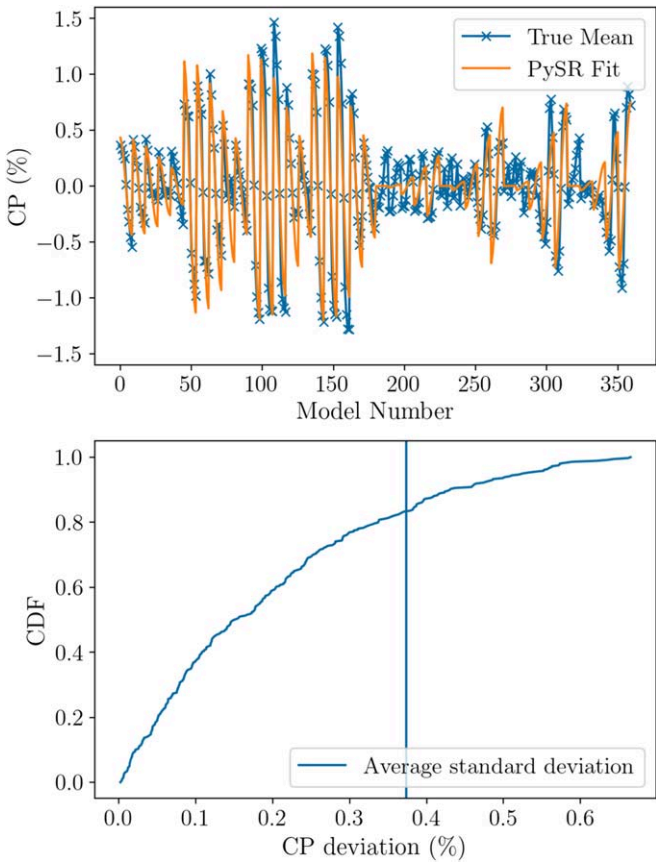


Figure 10. Top: performance of PySR fitting-function inferences for the means of Sgr A* MAD CP distributions. The model numbers span in the order of inclination, spin, R_{high} , and field configuration. Model numbers 0–180 correspond to aligned-field models, with 181–360 being reversed. Bottom: the cumulative distribution function of the L1 norm of error for the fitting function. The solid line is the average standard deviation of CP in the models.

All the best-bet models given in EHTC SgrA V fail the CP constraint. These are prograde MAD models with high R_{high} at

a low inclination. This can be attributed to the effect of black hole spin on prograde models, as mentioned in Section 5—cancellation between the $n=1$ photon ring and the $n=0$ “weakly lensed” emission shifts the distributions toward the center, while the observations are predominantly around the -1% level.

Given that $\theta > 90^\circ$ represents a clockwise rotation of the disk in the sky (beyond the ergosphere for retrograde models), there is a clear preference for retrograde MAD models in which the flow orientation is clockwise in the sky. All these models pass when the \mathbf{B} field is oriented parallel to the disk angular momentum vector (aligned field). This is because the photon ring has a negligible effect and the overall $n=0$ emission (in this configuration) is negative. These findings are consistent with the GRAVITY measurements of the orientation of the flow for Sgr A* based on the motion of NIR flares (GRAVITY Collaboration et al. 2018).

For the one passing prograde MAD model, the field is in the reversed configuration, meaning that all the passing MAD models have the dipole moment of the field pointed away from the observer. Given the combination of inclinations and field orientations, we find that the v_{net} constraint (on MADs) is sensitive to both the sense of rotation of the flow (as proposed and explored in Enßlin 2003 and Mościbrodzka et al. 2021, respectively) and the overall direction or structure of the magnetic field configuration (Beckert & Falcke 2002). If the constraint were insensitive to the sense of rotation of the flow, then models with $\theta < 90^\circ$ would pass, and if it were insensitive to the direction of the magnetic field, then both aligned and reversed fields for all passing MAD models would pass.

All the MAD edge-on inclination models fail, and only one of the SANE edge-on inclination models passes the CP constraint. This is because of cancellations that occur across the image domain, due to symmetries in the magnetic field structure for each of the models (Ricarte et al. 2021), yielding a net-zero CP fraction.

Combined with the constraints in EHTC SgrA V, the CP test eliminates all models. The best-bet prograde MAD models do

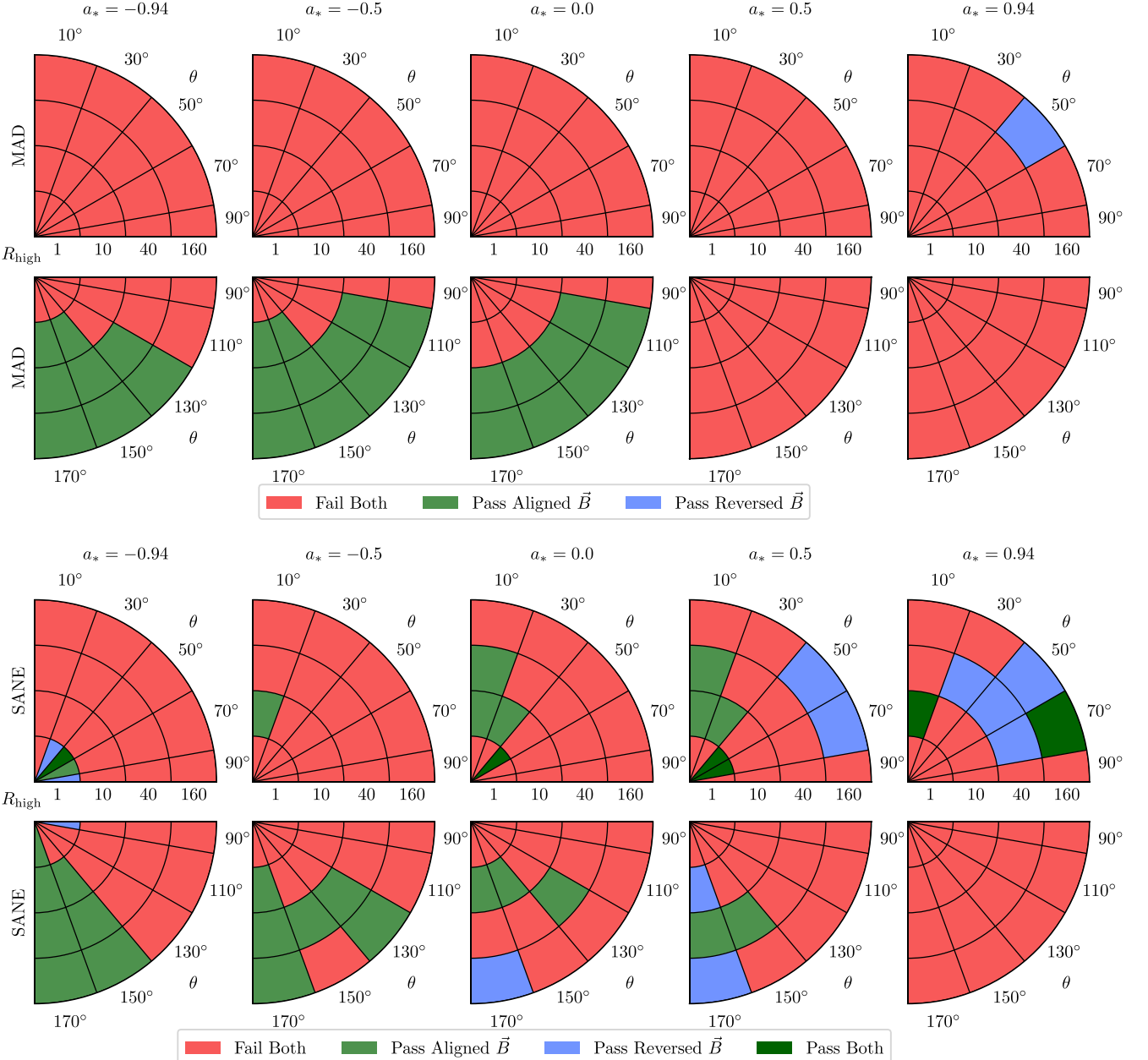


Figure 11. Pass/fail plots of the Illinois Sgr A* model library for v_{net} (top row: MAD models; bottom row: SANE models). Each pie plot represents a given spin, with R_{high} along the radial direction and the inclination (θ) as the polar angle of the subplot.

not produce sufficient CP, whereas the retrograde MADs (which pass CP constraints) are mostly eliminated from the m-ring constraints, which compare the ring width, asymmetry, and diameter of the model to the observed image. Most of the SANEs fail the m-ring and non-EHT (multiwavelength) constraints.

6.2. M87*

The CP measurements of M87* given in Goddi et al. (2021) constrain $|v_{\text{net}}| < 0.8\%$. This constraint was used for model comparison in EHTC M87 VIII, and most models aside from a few SANE models contained snapshots with v_{net} within this value. While the models used in this paper are from different GRMHD models evolved out to longer timescales, the underlying physics remains the same. Given the frequent v_{net}

sign fluctuations observed across all models, there exist a few snapshots where $|v_{\text{net}}| < 0.8\%$. A few SANE spin 0 models have only 2%–10% of snapshots passing this constraint, but most of the models have many passing snapshots, as the distributions are close to 0. The discerning power of v_{net} for M87*, while broadly consistent with the results of EHTC M87 VIII, does not reveal any significant trend.

While we do not apply the resolved CP upper limit of 3.7%, as given in EHTC M87 IX, we do not expect our results to be significantly different, as the GRMHD libraries contain the same underlying physics and differ mostly in the final integration time. EHTC M87 IX utilizes libraries of the reversed-field configuration and properties of the polarimetric quantities do not appear to vary significantly aside from v_{net} and the angle of the axisymmetric Fourier component of the EVPA ($\angle\beta_2$ in the paper), which is consistent with

expectations. Incorporating the additional parameter of the field configuration to the library, the outcome is not significantly changed, with MAD models with R_{low} 10 still preferred.

7. Discussion

Here we discuss certain limitations of the theoretical models and provide some expectations for future improvements. As these models are the same underlying GRMHD simulations used in the KHARMA library in EHTC SgrA V, most of the caveats discussed in that paper apply here. Given the diversity of the model parameters, it is difficult to predict the effect of an improvement on an entire library of simulations, and thus each of the suggestions merits a separate analysis that is beyond the scope of the paper.

The primary caveat is that the models are highly variable in Stokes I and V when compared to Sgr A*. While v_{net} for Sgr A* is consistently observed at the percent level, frequent sign crossings are observed for most models, due to turbulence and rapidly changing optical and Faraday depths. Comparing the mean of distributions could provide a more robust method of comparing simulations to observations (EHTC SgrA V; Wielgus et al. 2022a, 2024). However, for our models, the sign crossings invariably produce mean v_{net} values lower than the percent level. Improvements to physics in GRMHD models, such as including self-consistent electron heating and cooling mechanisms or the addition of leading-order collisionless corrections, such as viscosity and heat conduction, as given in Chandra et al. (2015), can potentially reduce the fluctuations of Stokes V in the models and thus shift the v_{net} distributions away from 0.

The initial condition of the current GRMHD library is an equilibrium Fishbone–Moncrief torus solution (Fishbone & Moncrief 1976) seeded with a magnetic field. Most of the emission regions for such simulations occur within 20M, with the time period chosen so as to allow these regions to reach a steady-state solution. However, alternative initial conditions, such as stellar-wind-fed models (Ressler et al. 2020), can yield qualitatively different results in all the Stokes images. Magnetic fields can greatly influence the structure of the CP image. Since the magnetization of the stellar winds is poorly constrained, qualitative features of the polarimetric image are sensitive to the choice of plasma β and further studies are necessary. For higher magnetizations of the stellar wind, the simulations can be expected to settle into a MAD state and show similar properties to the corresponding MAD simulation with similar inclinations and electron temperatures in our library.

Changes to GRMHD fluid parameters can influence the resulting v_{net} distributions. In a newer set of GRMHD simulations generated using KHARMA (referred to as “v5” as opposed to the current “v3”), the simulations are run with a different adiabatic index (5/3 instead of 4/3) for the fluid, different GRMHD floor prescriptions, a higher resolution (384 \times 192 \times 192 compared to 288 \times 128 \times 128 in v3), and are run out until $50 \times 10^3 GM/c^3$ in time. A comparison of the same GRRT model parameters between this simulation and the simulation used in the paper is given in Figure 12 (the same model as in Section 4). A two-sample K-S test cannot distinguish the newer simulation distribution from the one used in this paper, and both perform similarly when compared to observational data of Sgr A*, yet this inference cannot be applied to the full library of simulations. The characteristics of

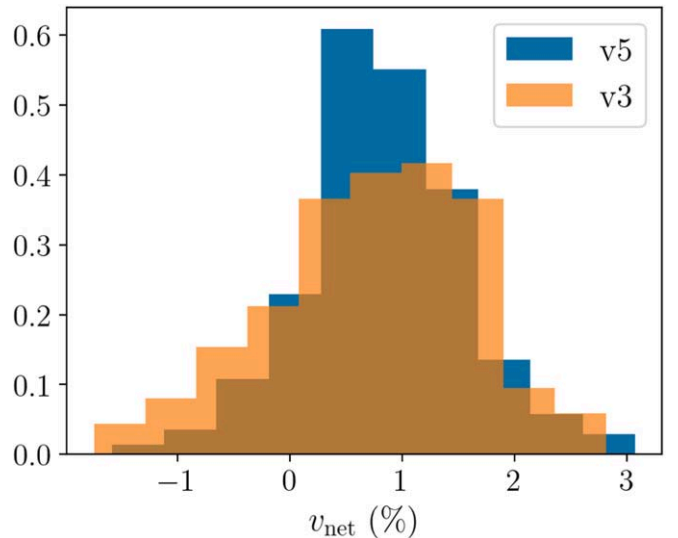


Figure 12. v_{net} distributions for a MAD $a+0.5$, R_{high} 40, and inclination 30° model with an aligned-field configuration for two different GRMHD simulations. “v3” is the simulation set used in this paper, while “v5” is a new image library with a higher GRMHD resolution (384 \times 192 \times 192 compared to 288 \times 128 \times 128 in v3) and different fluid adiabatic index (5/3 instead of 4/3). Both distributions are indistinguishable under a K-S test.

the new library, containing densely sampled black hole spins, will be discussed in a later paper.

Electron–positron plasmas have the capacity to greatly influence the morphology of the Stokes V image without affecting the Stokes I image significantly. With an equal proportion of positrons and electrons, both intrinsic emission and Faraday conversion through Faraday rotation vanish and the resultant CP will encode conversion through the sign of twist (Wardle et al. 1998; Anantua et al. 2020; Emami et al. 2021).

The eDF was chosen to be a relativistic Maxwell–Jüttner distribution. Based on observations of the solar wind and simulations of collisionless plasma simulations via particle-in-cell codes, a power-law tail to the distribution can be modeled—the so-called κ distribution (Kunz et al. 2015 and references therein). Nonthermal eDFs introduce hotter electrons that influence all the radiative transfer coefficients, but a systematic study of the effects on CP is still needed.

The R_{high} prescription (Mościbrodzka et al. 2016) used to assign electron temperatures in our models is a phenomenological model. The R_{high} model defines the electron temperatures as a particular function of plasma β . Another parameterization of the accretion flow is the critical beta model (Anantua et al. 2020), which differs in that the electron temperatures approach 0 instead of $1/R_{\text{high}}$ at high plasma β , in the midplane. Colder electrons in the midplane will enhance Faraday rotation while suppressing intrinsic emission and thus reduce v_{net} in the images.

As the observed v_{net} for Sgr A* seem to lie squarely around the -1% value across many decades, the potential effects of an external Faraday screen should be investigated (though recently argued against by Wielgus et al. 2024). Faraday conversion and intrinsic emission is heavily suppressed in cold plasmas compared to Faraday rotation, thus the existence of a screen should not greatly affect the v_{net} measurements. It is possible, however, for the screen to undergo field reversals along the photon trajectory, in which case Faraday conversion can

dominate in a small region where the field is perpendicular to the photon trajectory. Gruzinov & Levin (2019) investigate the effect of such field reversals in cold plasma and find that the resulting CP oscillates quasiperiodically as a function of λ^2 . Since the observations of Sgr A* do not seem to show this oscillation, we may assume that such effects are subdominant in observations of Sgr A*. For M87*, CP(λ) is not yet observed.

While $\sim 90\%$ of the emission up to 100 mas arises from horizon scales (EHTC SgrA II), emission from large-scale structures between 100 mas and 1 as is not as well constrained. The lack of a conclusively observed jet from Sgr A* at lower frequencies (EHTC SgrA II and references therein) also suggests that any extended emission is of low intensity. However, it is possible that a highly polarized, low-intensity source in this region could influence Stokes V measurements and offset a signal arising from the source. Future improvements to the global VLBI array can improve the limits on extended structure (Raymond et al. 2021).

8. Conclusion

In this paper, we investigate the CP of simulated images of Sgr A* and M87*, focusing on the image-integrated CP (v_{net}). We explore a library of GRMHD models spanning different black hole spins and accretion disk magnetic states (MAD and SANE). Ray-traced images of the GRMHD models span different electron temperatures, observer inclinations, and both aligned and reversed polarities of the global magnetic field. To understand the properties of v_{net} , we first focus on one MAD $a = +0.5$, $R_{\text{high}} = 160$, inclination 30° model. We then plot v_{net} distributions across an entire model library and find trends with respect to the library parameters along with fitting functions for the Sgr A* MAD models. Models of Sgr A* are constrained by performing a K-S test between simulations and unresolved ALMA observations of Sgr A*. We find the following results:

1. Field reversal does not flip v_{net} distributions, as there exist both symmetric and antisymmetric terms in the radiative transfer equation (Equation (4)). The relative contributions of these terms can vary greatly. Models with symmetric (antisymmetric) terms dominating the equation can have nearly symmetric (antisymmetric) distributions of v_{net} . In practice, however, most models contain contributions from both terms.
2. Large cancellations occur both spatially and temporally in CP due to turbulent fluctuations and symmetries in the magnetic field. Average images and means of v_{net} distributions can smooth over fluctuations and probe the structure of magnetic fields. The sense of twist of the magnetic field is encoded in the mean of the v_{net} distributions (when averaged over the field configuration). Inclinations $< 90^\circ$ encode an overall clockwise twist of field (positive v_{net}).
3. SANE models produce more CP on average than MADs. For Sgr A*, nearly all the MAD models lie within $|v_{\text{net}}| < 2\%$, whereas for SANEs this is $|v_{\text{net}}| \lesssim 5\%$.
4. When compared to v_{net} ALMA measurements of Sgr A* via a K-S test, the MAD models that pass contain \mathbf{B} pointing away from the observer. All but one of the passing models are clockwise in the sky, in agreement with the direction of the putative orbital motion reported by GRAVITY Collaboration et al. (2018) and Wielgus et al. (2022b). SANE models being more variable with

larger v_{net} tend to pass without a clear trend. None of the best-bet models survive the v_{net} constraint, as most of the MAD models exhibit sign changes in v_{net} , unlike observations, which lie closely around the -1% region.

5. Edge-on models produce $v_{\text{net}} \approx 0$, due to symmetries in the magnetic field structure, and are thus disfavored for Sgr A*.
6. The black hole spin influences the v_{net} distribution of a model. High-spin prograde models appear to contain imprints of the photon ring with the opposite sign of CP compared to the weakly lensed component, causing v_{net} in prograde models to be centered closer to 0 or even have the opposite sign, compared to otherwise similar retrograde models.
7. Electron temperature assignment can be constrained by future observations of the resolved CP measurement, $\langle |v| \rangle$. Higher- R_{high} models or colder electrons in the disk will have higher $\langle |v| \rangle$ values with v_{net} weakly affected.

Overall, we find that while CP in radiatively inefficient accretion flows can be complicated, there are interesting trends and properties with respect to model parameters. The GRMHD models appear to be highly variable in CP, with frequent sign crossings in v_{net} . The current constraints of v_{net} for Sgr A* seem to highlight the global direction of the magnetic field and the sense of rotation of the flow. Since v_{net} observations are possible for point sources, observational data from targets besides Sgr A* and M87* can also be used to infer model properties.

Acknowledgments

The authors thank Monika Mościbrodzka, Angelo Ricarte, and the anonymous EHT internal referee for valuable comments that improved the manuscript.

This work was supported by NSF grants AST 17-16327 (Horizon), OISE 17-43747, and AST 20-34306. This research used resources of the Oak Ridge Leadership Computing Facility at the Oak Ridge National Laboratory, which is supported by the Office of Science of the U.S. Department of Energy under Contract No. DE-AC05-00OR22725. This research used resources of the Argonne Leadership Computing Facility, which is a DOE Office of Science User Facility supported under Contract DE-AC02-06CH11357. This research was done using services provided by the OSG Consortium, which is supported by the National Science Foundation awards #2030508 and #1836650. This research is part of the Delta research computing project, which is supported by the National Science Foundation (award OCI 2005572) and the State of Illinois. Delta is a joint effort of the University of Illinois at Urbana-Champaign and its National Center for Supercomputing Applications. This paper makes use of the following ALMA data: ADS/JAO.ALMA#2013.1.00764.S, ADS/JAO.ALMA#2016.1.01154.V, and ADS/JAO.ALMA#2016.1.01404.V. ALMA is a partnership of ESO (representing its member states), NSF (USA) and NINS (Japan), together with NRC (Canada), NSC and ASIAA (Taiwan), and KASI (Republic of Korea), in cooperation with the Republic of Chile. The National Radio Astronomy Observatory is a facility of the National Science Foundation operated under cooperative agreement by Associated Universities, Inc. C.F.G. was supported by the IBM Einstein Fellow Fund at the Institute for Advanced Study. M.W. acknowledges the support from the European Research Council advanced grant “M2FINDERS—

Mapping Magnetic Fields with INterferometry Down to Event hoRizon Scales” (grant No. 101018682).

Appendix A One-zone Model Stokes V versus Frequency

In the optically/Faraday-thin limit, we can approximate the contributing terms (intrinsic emission and Faraday conversion) to Stokes V from the full solution of the radiative transfer equation (Equation (3)) as follows:

$$V_{\text{emission}} \approx j_V L, \quad (\text{A1})$$

$$V_{\text{conversion}} \approx \rho_Q \rho_V j_Q L^3, \quad (\text{A2})$$

where Stokes V from Faraday conversion in a uniform field geometry only arises from Faraday conversion of linearly polarized light rotated from Q to U . L is a characteristic length scale, which we set to the radius of the one-zone sphere $L = 5GM/c^2$. Thus, Equations (A1) and (A2) can be used as proxies to probe the general spectral behavior of the components to the full solution of Stokes V .

Figure 13 shows the spectral behavior of the two CP mechanisms along with their approximations in the Faraday-thin limit using one-zone models of Sgr A*. The Stokes V_{emission} ($V_{\text{conversion}}$) solution is obtained by setting $\rho_Q = 0$ ($j_V = \alpha_V = 0$), respectively. The approximations have the same scaling behavior as the full solutions, with the CP from Faraday conversion decreasing much faster with frequency than intrinsic emission.

When comparing with numerical models, we see the same qualitative behavior: models in which intrinsic emission is expected to dominate show a slower decrease in frequency compared to conversion-dominated models. The spectral slopes of Stokes V are completely different, but this is not unexpected, given the nontrivial field configuration of the simulations and the integration across many different geodesics (compared to a single geodesic in the analytic solution).

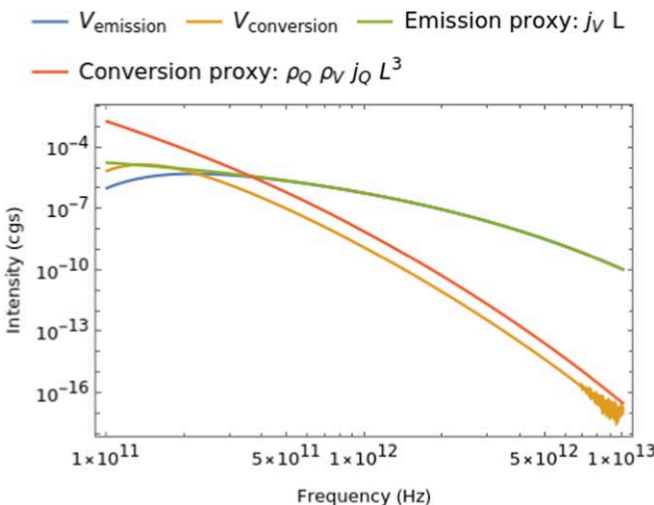


Figure 13. Stokes V vs. frequency for solutions to the radiative transfer equation consisting of either only intrinsic emission (V_{emission}) or Faraday conversion ($V_{\text{conversion}}$), in the Faraday-thin limit. Estimates to these solutions (proxies) from dimensional analysis of the components are also plotted and display the same scaling behavior as the corresponding solution.

Appendix B Validity of Fractional CP Distribution

Before making estimates and predictions from the surveyed data, it should be tested that the distributions computed from the EHT imaging library have converged to the true distribution of the process. Here, we investigate the convergence properties of the models with respect to resolution in time, GRMHD, and GRRT modeling.

Have the distributions converged, i.e., has the library been imaged over a long enough interval? Figure 14 displays the effect of increasing the simulation time for our sample MAD, spin $+0.5$, $R_{\text{high}} 160$, inclination 30° model. While the mean of the distribution is not fully settled, the changes are within 10%: from 5 to 15 kM time intervals, in increments of 3 kM, the mean v_{net} changes as 0.51%, 0.78%, 0.67%, 0.79%, and 0.82%, respectively. The distributions also become more unimodal as the number of independent samples increases. The correlation time of this model is about 400M, implying about 38 independent samples and a standard error of $\sigma/\sqrt{n} \approx 0.13\%$.

The distributions might have encoded features dependent on the resolution of the GRMHD simulations. Figure 15 shows that this is not the case for a MAD spin $+0.94$ model, as the resolution does not drastically affect the distribution. The GRMHD resolution used for the EHT imaging in EHTC SgrA V and this paper was $288 \times 128 \times 128$. The fluctuations in the distributions are likely due to limited time sampling of the model (both in cadence and length).

v_{net} is a metric that is independent of the image (GRRT) resolution past a certain threshold that represents the scale of critical structures in the image. We generate a snapshot for a MAD spin $+0.94$ model at resolutions $0.25, 0.5, 1, 2, 4, 8$, and $16 \mu\text{as pixel}^{-1}$ and find the v_{net} values to be 0.361%, 0.358%, 0.340%, 0.384%, 0.476%, 0.447%, and 0.335%, respectively. Downsampling the model library ($0.5 \mu\text{as pixel}^{-1}$) across all parameters shows similar trends, suggesting that the v_{net} measurements of GRRT models usually vary within 0.1% across image resolution until $8 \mu\text{as pixel}^{-1}$, making the existing image resolution of the library sufficient.

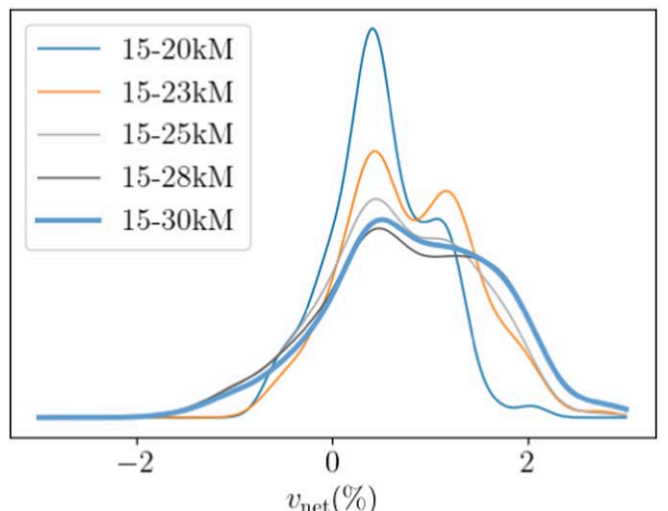


Figure 14. CP distributions for an Sgr A* MAD, spin $+0.5$, $R_{\text{high}} 160$, inclination 30° model for larger time ranges. While the distribution has not fully converged, the fluctuations in the mean are relatively low. The mean values for each distribution with increasing time range are: 0.51%, 0.78%, 0.67%, 0.79%, and 0.82%, respectively. The total distribution used for analyses is given by the thick light blue line.

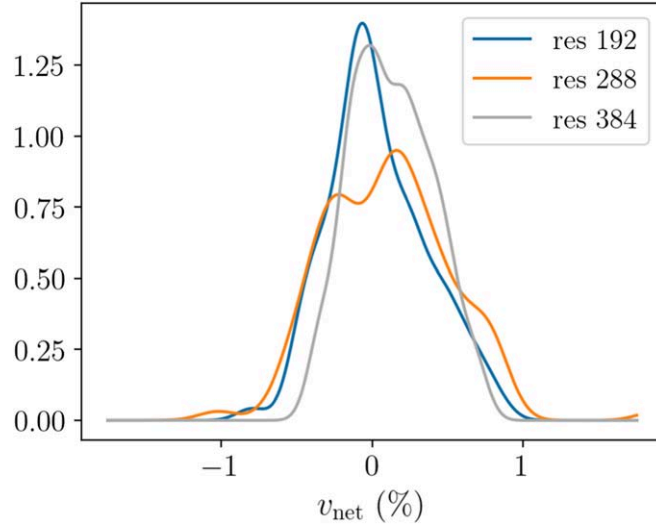


Figure 15. Kernel density estimation PDFs for different GRMHD simulation resolutions for a spin $+0.94$ MAD model with M87* parameters. The full resolutions of each of the distributions (radial x poloidal x azimuthal) are $192 \times 96 \times 96$, $288 \times 128 \times 128$, and $384 \times 192 \times 192$, respectively. This demonstrates that resolution does not influence the distributions significantly.

Appendix C M87* v_{net} Plots

Figures 16 and 17 show v_{net} distributions for the M87* library parameters. As the observer inclination for the M87* library is fixed to the inclination angle of the forward jet, these M87* distributions are mostly a subset of the parameters used

for Sgr A*, aside from a denser sampling of R_{high} . Thus, inferences on the parameter trends based on the Sgr A* distributions also apply to M87*: SANEs produce more v_{net} than the MAD models, the shift of the v_{net} distributions goes toward 0 as the spin goes from negative to positive, and an increase in R_{high} increases and broadens the v_{net} distributions.

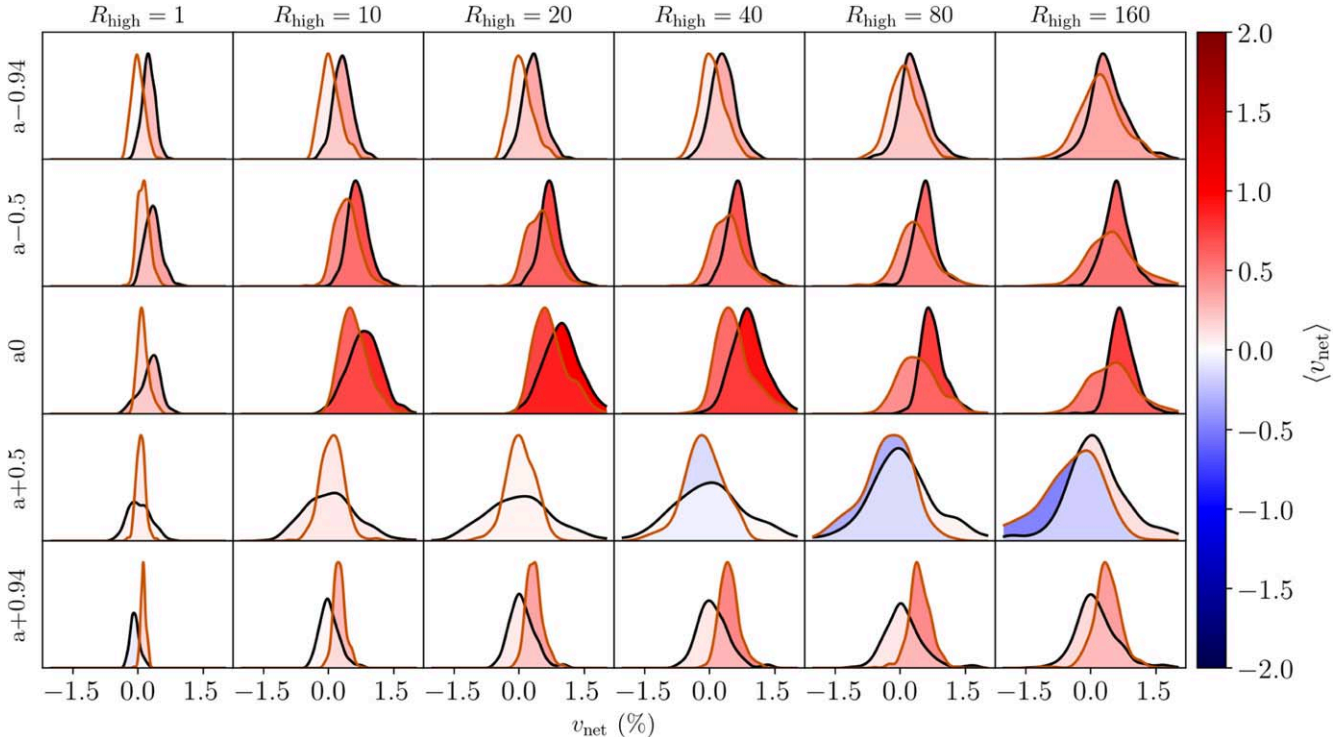


Figure 16. Distributions of v_{net} for all the MAD M87* models. The Y-axis corresponds to spin. The X-axis corresponds to R_{high} . The inclination is 163° for $a_* \geq 0$ and 17° otherwise. The black (orange) lines represent the aligned- (reversed-) field distribution, respectively. The color filled within the distributions is their mean v_{net} and the overlapping regions are the mean v_{net} of both field distributions combined. The height of each subplot is adjusted to fix the maximum height constant for visualization purposes.

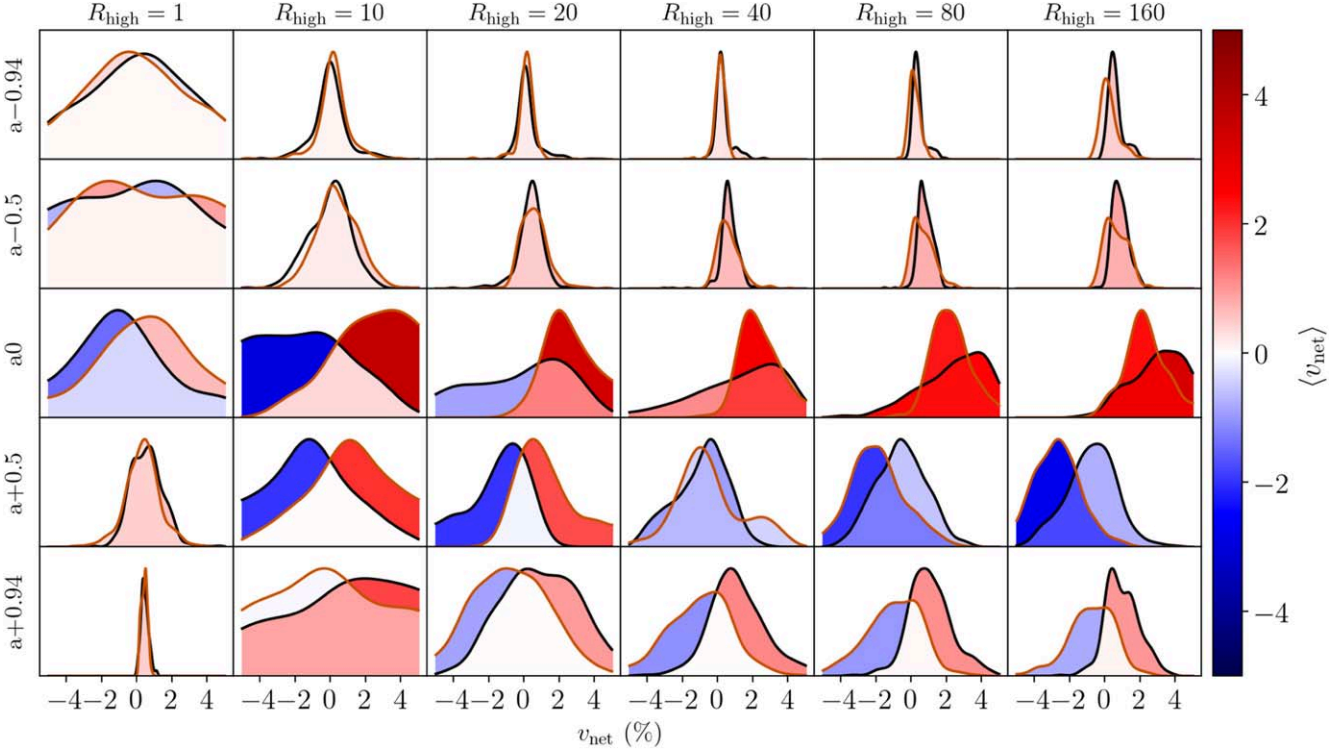


Figure 17. The same as Figure 16, except for SANE distributions.

Appendix D CP Distribution Tables

Here, we provide tables of the first two moments of the distributions for v_{net} (%) for both Sgr A* and M87* in Table 2.

Table 2
Mean and Standard Deviation for v_{net} (Fractional CP, %) for all GRMHD Models for SgrA* and M87*

Source	Flux	a	R_{high}	θ	Mean v_{net}	Std v_{net}	Mean v_{net} (Rev B)	Std. v_{net} (Rev B)
SgrA*	SANE	-0.94	1	10	0.62	2.80	-0.15	2.85
SgrA*	SANE	-0.94	1	30	-0.71	1.32	-1.00	1.36
SgrA*	SANE	-0.94	1	50	-1.61	1.96	-1.96	2.01
SgrA*	SANE	-0.94	1	70	-1.66	2.38	-2.16	2.49
...
M87*	MAD	+0.94	40	163	0.09	0.36	0.45	0.23
M87*	MAD	+0.94	80	163	0.08	0.44	0.45	0.26
M87*	MAD	+0.94	160	163	0.13	0.48	0.37	0.33

(This table is available in its entirety in machine-readable form in the [online article](#).)

ORCID iDs

Abhishek V. Joshi [DOI](https://orcid.org/0000-0002-2514-5965) <https://orcid.org/0000-0002-2514-5965>
 Ben S. Prather [DOI](https://orcid.org/0000-0002-0393-7734) <https://orcid.org/0000-0002-0393-7734>
 Chi-kwan Chan [DOI](https://orcid.org/0000-0001-6337-6126) <https://orcid.org/0000-0001-6337-6126>
 Maciek Wielgus [DOI](https://orcid.org/0000-0002-8635-4242) <https://orcid.org/0000-0002-8635-4242>
 Charles F. Gammie [DOI](https://orcid.org/0000-0001-7451-8935) <https://orcid.org/0000-0001-7451-8935>

References

Anantua, R., Emami, R., Loeb, A., & Chael, A. 2020, *ApJ*, **896**, 30
 Anantua, R., Ressler, S., & Quataert, E. 2020, *MNRAS*, **493**, 1404
 Beckert, T., & Falcke, H. 2002, *A&A*, **388**, 1106
 Bower, G. C., Broderick, A., Dexter, J., et al. 2018, *ApJ*, **868**, 101
 Chandra, M., Gammie, C. F., Foucart, F., & Quataert, E. 2015, *ApJ*, **810**, 162
 Cranmer, M. 2020, PySR: Fast and Parallelized Symbolic Regression in Python/Julia, v0.2, Zenodo, doi:[10.5281/zenodo.4041459](https://doi.org/10.5281/zenodo.4041459)
 Cranmer, M., Sanchez-Gonzalez, A., Battaglia, P., et al. 2020, arXiv:[2006.11287](https://arxiv.org/abs/2006.11287)
 Dexter, J. 2016, *MNRAS*, **462**, 115
 Emami, R., Anantua, R., Chael, A. A., & Loeb, A. 2021, *ApJ*, **923**, 272
 Enßlin, T. A. 2003, *A&A*, **401**, 499
 Event Horizon Telescope Collaboration, Akiyama, K., Alberdi, A., et al. 2019a, *ApJL*, **875**, L1
 Event Horizon Telescope Collaboration, Akiyama, K., Alberdi, A., et al. 2019b, *ApJL*, **875**, L2
 Event Horizon Telescope Collaboration, Akiyama, K., Alberdi, A., et al. 2019c, *ApJL*, **875**, L3
 Event Horizon Telescope Collaboration, Akiyama, K., Alberdi, A., et al. 2019d, *ApJL*, **875**, L4
 Event Horizon Telescope Collaboration, Akiyama, K., Alberdi, A., et al. 2019e, *ApJL*, **875**, L5
 Event Horizon Telescope Collaboration, Akiyama, K., Alberdi, A., et al. 2019f, *ApJL*, **875**, L6
 Event Horizon Telescope Collaboration, Akiyama, K., Algaba, J. C., et al. 2021a, *ApJL*, **910**, L12
 Event Horizon Telescope Collaboration, Akiyama, K., Algaba, J. C., et al. 2021b, *ApJL*, **910**, L13
 Event Horizon Telescope Collaboration, Akiyama, K., Alberdi, A., et al. 2022a, *ApJ*, **930**, L12
 Event Horizon Telescope Collaboration, Akiyama, K., Alberdi, A., et al. 2022b, *ApJ*, **930**, L13
 Event Horizon Telescope Collaboration, Akiyama, K., Alberdi, A., et al. 2022c, *ApJ*, **930**, L14
 Event Horizon Telescope Collaboration, Akiyama, K., Alberdi, A., et al. 2022d, *ApJ*, **930**, L15
 Event Horizon Telescope Collaboration, Akiyama, K., Alberdi, A., et al. 2022e, *ApJ*, **930**, L16
 Event Horizon Telescope Collaboration, Akiyama, K., Alberdi, A., et al. 2022f, *ApJ*, **930**, L17
 Event Horizon Telescope Collaboration, Akiyama, K., Alberdi, A., et al. 2023, *ApJ*, **957**, L20
 Fishbone, L. G., & Moncrief, V. 1976, *ApJ*, **207**, 962
 Gammie, C. F., McKinney, J. C., & Tóth, G. 2003, *ApJ*, **589**, 444
 Goddi, C., Martí-Vidal, I., Messias, H., et al. 2021, *ApJL*, **910**, L14
 GRAVITY Collaboration, Abuter, R., Amorim, A., et al. 2018, *A&A*, **618**, L10
 Gruzinov, A., & Levin, Y. 2019, *ApJ*, **876**, 74
 Hamaker, J. P., & Bregman, J. D. 1996, *A&AS*, **117**, 161
 Homan, D. C., Lister, M. L., Aller, H. D., Aller, M. F., & Wardle, J. F. C. 2009, *ApJ*, **696**, 328
 Igumenshchev, I. V., Narayan, R., & Abramowicz, M. A. 2003, *ApJ*, **592**, 1042
 Johnson, M. D., Lupsasca, A., Strominger, A., et al. 2020, *SciA*, **6**, eaaz1310
 Jones, T. W., & O'Dell, S. L. 1977, *ApJ*, **214**, 522
 Kunz, M. W., Schekochihin, A. A., Chen, C. H. K., Abel, I. G., & Cowley, S. C. 2015, *JPIPh*, **81**, 325810501
 Landi Degl'Innocenti, E., & Landi Degl'Innocenti, M. 1985, *SoPh*, **97**, 239
 Marszewski, A., Prather, B. S., Joshi, A. V., Pandya, A., & Gammie, C. F. 2021, *ApJ*, **921**, 17
 Mościbrodzka, M., Falcke, H., & Shiokawa, H. 2016, *A&A*, **586**, A38
 Mościbrodzka, M., & Gammie, C. F. 2018, *MNRAS*, **475**, 43
 Mościbrodzka, M., Janiuk, A., & De Laurentis, M. 2021, *MNRAS*, **508**, 4282
 Muñoz, D. J., Marrone, D. P., Moran, J. M., & Rao, R. 2012, *ApJ*, **745**, 115
 Narayan, R., Igumenshchev, I. V., & Abramowicz, M. A. 2003, *PASJ*, **55**, L69
 Narayan, R., Sładowski, A., Penna, R. F., & Kulkarni, A. K. 2012, *MNRAS*, **426**, 3241
 Pandya, A., Chandra, M., Joshi, A., & Gammie, C. F. 2018, *ApJ*, **868**, 13
 Pandya, A., Zhang, Z., Chandra, M., & Gammie, C. F. 2016, *ApJ*, **822**, 34
 Penrose, O. 1960, *PhFl*, **3**, 258
 Prather, B. 2022, PhD thesis, Univ. of Illinois at Urbana-Champaign, <https://hdl.handle.net/2142/117717>
 Prather, B. 2024, KHARMA, v1, Zenodo, doi:[10.5281/zenodo.12107141](https://doi.org/10.5281/zenodo.12107141)
 Quataert, E., & Gruzinov, A. 1999, *ApJ*, **520**, 248
 Raymond, A. W., Palumbo, D., Paine, S. N., et al. 2021, *ApJS*, **253**, 5
 Ressler, S. M., Tchekhovskoy, A., Quataert, E., Chandra, M., & Gammie, C. F. 2015, *MNRAS*, **454**, 1848
 Ressler, S. M., White, C. J., Quataert, E., & Stone, J. M. 2020, *ApJL*, **896**, L6
 Ricarte, A., Qiu, R., & Narayan, R. 2021, *MNRAS*, **505**, 523
 Sładowski, A., Narayan, R., Penna, R., & Zhu, Y. 2013, *MNRAS*, **436**, 3856
 Tsunetoe, Y., Mineshige, S., Ohsuga, K., Kawashima, T., & Akiyama, K. 2021, *PASJ*, **73**, 912
 Wardle, J. F. C., Homan, D. C., Ojha, R., & Roberts, D. H. 1998, *Natur*, **395**, 457
 Wielgus, M., Issaoun, S., Martí-Vidal, I., et al. 2024, *A&A*, **682**, A97
 Wielgus, M., Marchili, N., Martí-Vidal, I., et al. 2022a, *ApJL*, **930**, L19
 Wielgus, M., Mościbrodzka, M., Vos, J., et al. 2022b, *A&A*, **665**, L6
 Wilson, A. S., & Weiler, K. W. 1997, *ApJ*, **475**, 661
 Wong, G. N., Prather, B. S., Dhruv, V., et al. 2022, *ApJS*, **259**, 64
 Yuan, F., & Narayan, R. 2014, *ARA&A*, **52**, 529
 Zhdankin, V., Uzdensky, D. A., & Kunz, M. W. 2021, *ApJ*, **908**, 71